Regional impacts of iron-light colimitation in a global biogeochemical model

Eric D. Galbraith[1], Anand Gnanadesikan[2], John P. Dunne[2], Michael R. Hiscock[1]

1: AOS Program, Princeton University, Princeton, NJ 08544

2: NOAA Geophysical Fluid Dynamics Laboratory, Princeton, NJ 08542

Manuscript in preparation for Biogeosciences

Abstract

Laboratory and field studies have revealed that iron has multiple roles in phytoplankton physiology, with particular importance for light-harvesting cellular machinery. However, although iron-limitation is explicitly included in numerous biogeochemical/ecosystem models, its implementation varies, and its effect on the efficiency of light harvesting is often ignored. Given the complexity of the ocean environment, it is difficult to predict the consequences of applying different iron limitation schemes. Here we explore the interaction of iron and nutrient cycles using a new, streamlined model of ocean biogeochemistry. Building on the photoadaptation model of Geider et al. (1997) and the parameterized export model of Dunne et al. (GBC, 2005), the Biology Light Iron Nutrients and Gasses (BLING) model is constructed with only three explicit tracers but including macronutrient and micronutrient limitation, light limitation, photoadaptation, and an implicit treatment of community structure. The structural simplicity of this model allows us to clearly isolate the global effects of iron availability on maximum light-saturated photosynthesis rates from the effects on photosynthetic efficiency. We find that the effect on light-saturated photosynthesis rates is dominant, negating the importance of photosynthetic efficiency in most regions, especially the cold waters of the Southern Ocean. The primary exceptions to this occur in iron-rich regions of the northern hemisphere, where high light-saturated photosynthesis rates cause photosynthetic efficiency to play a more important role. Additionally, we speculate that the small phytoplankton dominating iron-limited regions tend to have relatively high

22 photosynthetic efficiency, such that iron-limitation has less of a deleterious effect on
23 growth rates than would be expected from short-term iron addition experiments.
24

Introduction

In large surface regions of the open ocean, macronutrients remain in considerable abundance throughout the year, a puzzle that has engaged the interest of oceanographers for many decades. These regions contrast with coastal environments in which the surface ecosystem handily strips out macronutrients, despite high resupply rates. Although many factors have been implicated in the maintenance of the nutrient-rich surface oceans, limitation by micronutrients – principally iron – clearly plays a central role.

Over the past decades, numerous experiments have shown that adding iron to macronutrient-rich regions of the ocean produces plankton blooms (see Boyd et al. 2007 for a review). On a physiological level, this appears to be largely due to the role of iron in the electron transport pathways that accomplish photosynthesis (Raven, 1990; Maldonado et al., 1999); cells that are replete in iron can build more photosynthetic reaction centers and utilize the light they collect more efficiently (Greene et al., 1991; Strzepek and Harrison, 2004). Iron is also required for other cellular processes, including the reduction of nitrate to ammonia (Raven, 1990; Price et al., 1991). Laboratory studies support this, reporting large decreases in growth rates under iron limitation (Price et al, 1991; Greene et al., 1991; Sunda and Huntsman, 1995; Timmermans et al., 2004). In addition, iron deficiency has been shown to significantly reduce the chlorophyll to carbon ratio, θ, in almost all cases, due to the requirement for iron in chlorophyll biosynthesis (e.g. Greene et al., 1991; Sunda and Huntsman, 1995; Marchetti et al., 2007).

While the impact of iron on photosynthesis is clearly important, the manner in which its effects should be implemented in numerical models is less clear. Recent representations of algal physiology in biogeochemical models have often relied on the

47 photoadaptation scheme of Geider et al. (1997), used in numerous global models (e.g.
48 Moore and Doney, 2002; Aumont and Bopp, 2006). This scheme is built around a
49 common expression for the carbon-specific photosynthesis rate, P^C, as a function of
50 irradiance, I,

51 $$P^C = P_m^C \{1 - \exp(-I/I_k)\} \quad (1)$$

52 where P_m^C is a macronutrient-limited, temperature-dependent, light-saturated carbon-
53 specific photosynthesis rate (s^{-1}) and I_k is a scaling term that determines the degree of
54 light-limitation (W m^{-2}). Note that photosynthesis is always light limited to some degree
55 in this formulation (since $\{1 - \exp(-I/I_k)\}$ is always less than 1), and that for a given I,
56 photosynthesis decreases with increasing I_k. In the model of Geider et al. (1997), θ adapts
57 to a phytoplankter's nutritional status, temperature, and light environment in a way that is
58 consistent with laboratory experiments. This leads to a formulation for I_k as a function of
59 P_m^C, θ, and α^{chl}, the latter of which is the initial slope of the chlorophyll-*a* specific
60 photosynthesis-light response curve (units of g C g chl^{-1} W^{-1} m^2 s^{-1}). This latter term
61 governs how rapidly photosynthesis (relative to chlorophyll) increases with increasing
62 light at low light levels, essentially a metric for the yield of usable photons harvested by
63 each molecule of chorophyll under low light (Frenette et al., 1993; Hancke et al., 2008).
64 Substituting the Geider et al. (1997) formulation for θ in their equation for I_k, we
65 rearrange to obtain

66 $$I_k = \frac{P_m^C}{\alpha^{chl}\theta_{\max}} + \frac{I_{mem}}{2} \quad (2)$$

67 where $\theta_{\max}$ is a maximum chlorophyll-to-carbon ratio (g chl gC^{-1}) and I_{mem} is the
68 irradiance to which the phytoplankton are accustomed. This equation captures the

69 capacity of phytoplankton to adjust their photosynthetic machinery to their environment,
70 in order to maximize photosynthesis rates while minimizing metabolic costs.

71 Within this widely-applied conceptual framework, the experimental evidence
72 suggests that iron limitation could impact the growth of phytoplankton in three obvious
73 ways. First, it could reduce the light-saturated growth rate P_m^C. This would represent the
74 need for iron in proteins that mediate photosynthetic electron transport (Raven, 1990) and
75 thereby determine the maximum yield of electrons for photosynthesis when light is
76 abundant. Additionally, this term accounts for the utility of iron for non-photosynthetic
77 processes such as nitrate reduction (Price et al., 1991). However, if P_m^C is the only iron-
78 dependent term, low iron will have the effect of making the plankton less light-limited, as
79 they will need less light to match the other cellular functions (see the first term of eq. 2).
80 In other words, because Fe limitation reduces the maximum achievable photosynthetic
81 rate, the utility of photons would decrease under Fe limitation, making light availability
82 less important. This tendency would be counteracted by including iron dependencies in
83 the two other obvious terms: α^{chl}, so that photosynthetic efficiency decreases at low light
84 under iron limitation, representing a reduction of the reaction centers available for light
85 harvesting elements; and $\theta_{\max}$, so that iron deficiency reduces chlorophyll synthesis and
86 thereby cause $\theta_{\max}$ to decrease. Note that the second and third mechanisms are
87 numerically linked in the photosynthesis formulation, through modification of I_k as the
88 product $1/\alpha^{chl}\theta_{\max}$.

89 Applying iron dependencies to these three terms appears to broadly reflect the
90 available measurements of photosynthetic parameters made during bottle incubations and
91 mesoscale iron fertilization experiments. For example, in bottle incubations of natural

92 samples from the Drake Passage, Hopkinson et al. (2007) reported that iron addition
93 increased α^{chl}, θ and P_m^B (the light-saturated chlorophyll-specific growth rate, equal to
94 P_m^C/θ). Marchetti et al. (2006) also reported large increases in these three parameters,
95 within an iron-fertilized patch of the subarctic Pacific during the SERIES experiment.
96 Hiscock et al. (2008) presented observations from the SOFeX mesoscale iron enrichment
97 experiment, showing an increase of α^{chl} by about 70% while quantum yield (effectively α
98 $^{chl}\theta$) increased by about twice as much, a factor of ~2.5. However, in their case the
99 chlorophyll-specific photosynthesis rate P_m^B remained relatively unchanged, indicating
100 that any change in P_m^C was approximately balanced by a corresponding change in θ.
101 Taken together, these results suggest that P_m^C, θ and α^{chl} can all change significantly as a
102 function of Fe availability, although the magnitudes of the changes vary. However, many
103 biogeochemical models only include the effect of iron on P_m^C, while variation in θ and α
104 ^{chl} may arise indirectly, through changes in plankton composition (for models in which
105 plankton functional types have different photosynthetic parameters), or not at all. Hence,
106 it is useful to understand how including an iron dependency for each of these three
107 photosynthetic parameters affects global biogeochemical cycling.
108 Although including additional iron limitation terms within the photosynthesis
109 formulation is relatively straightforward, understanding their net impact on a global
110 model is not. Introducing iron limitation alters the spatiotemporal distribution of
111 nutrients, chlorophyll, and biomass in a way that will depend on the representation of
112 grazing and export, the physical circulation regime, and the iron cycle itself.
113 Understanding the dynamics of iron limitation at the global scale requires global models
114 that consider both realistic physical transport and biology, and which can be deliberately

115 manipulated in order to target isolated components of the problem. However,
116 comprehensive state-of-the-art biogeochemical schemes used in earth system modeling
117 typically include multiple functional groups with differing responses to iron and nutrient
118 limitation, complex zooplankton dynamics (Aumont et al., 2003), interactions between
119 nitrogen fixation and iron limitation (Doney et al., 2007, Moore et al. 2007), and
120 interactions between the global oxygen cycle and nutrient limitation via denitrification
121 (Schmittner et al., 2006), all of which introduce complicating feedbacks.
122 This paper presents a new model of global biogeochemical cycling
123 (Biogeochemistry-with-Light-Iron-Nutrients-Gas or BLING) that includes a
124 physiologically-based representation of light limitation and explicitly simulates limitation
125 by both iron and a macronutrient, but parameterizes the net effects of community size
126 structure, grazing, and export following the work of Dunne et al. (2005). Thus, it presents
127 a reasonable framework in which to isolate the physiological effects of iron limitation,
128 without nonlinear interactions between ecosystem components and other elemental
129 cycles. The model is described in detail in Section 2. We then describe a series of
130 experiments in which we isolate the impacts of iron dependencies on the global
131 biogeochemical simulation, as described in Sections 3. Section 4 concludes the paper.
132

133 **2. Model description**

134 BLING was developed as an intermediary between complex, highly nonlinear
135 biogeochemical-ecosystem models (e.g. Moore et al., 2004; Aumont and Bopp, 2006)
136 and simple, idealized biogeochemical models, that either ignore representation of
137 ecosystem dynamics (e.g. Dutkiewicz et al., 2005; Doney et al., 2006) or that generate

export production by forcing surface nutrients towards observations (e.g. Najjar and Orr, 1999; Gnanadesikan et al., 2002, 2004). Like these other coupled ocean-biogeochemical models, BLING is designed to be embedded within an ocean general circulation model, and produces a three dimensional solution that changes with time according to the physical ocean environment. BLING uses a relatively complex growth and export formulation, and is fully prognostic, in that the output depends only on in situ parameters provided by a physical circulation model, without restoring to observations. It is also 'continuous', in that all equations are solved in all grid cells, with no arbitrary division between a shallow interval of export production and a remineralizing deep ocean; this allows ocean metabolism to arise purely from the physical forcing. Despite these features, the model only requires three explicit tracers, which we call dissolved inorganic phosphorus (PO_4), dissolved organic phosphorus (DOP) and dissolved iron (Fe). It achieves this by treating the ecosystem implicitly, i.e. without any tracers that explicitly represent organisms. The core behavior of the model can therefore be thought of as an 'NPZD' (nutrient, phytoplankton, zooplankton and detritus) model where the P, Z and D tracers are treated implicitly, so that computationally it is simply an 'N' model. As discussed below, the remineralization is dependent on the oxygen concentration. For this reason, as well as to better understand impacts of changes in productivity, we also carry an oxygen (O_2) tracer for a total of four prognostic tracers (Figure 1). As a result, BLING is suitable for use in well-resolved physical models that include mixed-layer dynamics and a diurnal cycle, while remaining less complex and less computationally intensive than full ecosystem models.

161 *a.) Growth rate formulation*

162 The growth rate of phytoplankton (μ) is calculated as a function of the ambient
163 water characteristics: nutrient concentrations, light, and temperature. While the
164 macronutrient- and temperature-dependent formulations used here are very typical of
165 biogeochemical-ecosystem models, we use a novel scheme for representing iron
166 limitation that does not rely exclusively on Liebig's law of the minimum (by which only
167 the most limiting nutrient affects growth) but also incorporates nutrient-light co-
168 limitation in a way that is broadly consistent with laboratory and field studies of
169 phytoplankton.

170 The growth rate calculation begins by determining the light-saturated
171 photosynthesis rate from the *in situ* conditions,

172 $$P_m^C = P_0^C \times \exp(kT) \times \min\left(Def_{fe}, \frac{PO_4}{K_{PO4} + PO_4}\right) \quad (5a)$$

173 which depends on a specified maximum photosynthesis rate at temperature T=0°C (P_0^C),
174 a temperature-dependent term with k=0.063 °C^{-1} following Eppley (1972), and a
175 limitation by iron and phosphate following Liebig's law of the minimum. Phosphate
176 limitation is given by the simple Monod relationship as shown, which depends only on
177 the half-saturation constant K_{PO4}, while Fe limitation is expressed by the term Def_{fe} as
178 described below.

179 In calculating Def_{Fe} we represent the fact that, in contrast to nitrogen and carbon,
180 Fe is taken up by phytoplankton in a highly variable ratio to phosphorus (e.g. Sunda &
181 Huntsman, 1997, Marchetti et al., 2006b, Boyd et al., 2007). We calculate this uptake
182 ratio directly from the ambient water chemistry as

183 $$(Fe:P)_{uptake} = (Fe:P)_0 * \frac{Fe}{K_{fe} + Fe} \quad (3)$$

184 where Fe is the dissolved iron concentration, $(Fe:P)_0$ is a maximal uptake ratio and K_{fe}
185 defines the half-saturation constant for the uptake ratio. Although very simple, this
186 formulation results in a correlation between $(Fe:P)_{uptake}$ and dissolved Fe concentrations
187 that approximates the response shown in laboratory studies such as that of Sunda and
188 Huntsman (1997). Since, for balanced growth, the uptake ratio is equal to the cell quota,
189 we can calculate iron limitation directly from $(Fe:P)_{uptake}$,

190 $$Def_{Fe} = \frac{(Fe:P)_{uptake}}{K_{Fe:P} + (Fe:P)_{uptake}} \times \frac{K_{Fe:P} + (Fe:P)_0}{(Fe:P)_0} \quad (4)$$

191 where $K_{Fe:P}$ defines the half-saturation cellular Fe:P quota, i.e. the ratio at which the iron
192 limitation term equals 0.5. The second term in equation 4 normalizes the expression, so
193 that at high concentrations of dissolved iron, Def_{Fe} approaches 1. Treating uptake in this
194 fashion allows the implicit cellular Fe:P to increase as Fe concentrations increase, but
195 with diminishing physiological returns, consistent with the notion of 'luxury' uptake
196 (Sunda and Huntsman, 1995; Marchetti et al., 2009).

197 Iron limitation can also be applied to two additional components of the general
198 Geider et al. (1997) photosynthesis rate formulation, introduced in eq. 2 above, as
199 follows:

200 $$\alpha^{chl} = \alpha_{\min}^{chl} + (\alpha_{\max}^{chl} - \alpha_{\min}^{chl}) \times Def_{Fe} \quad (5b)$$

201 $$\theta_{\max}^{Fe} = \theta_{\min} + (\theta_{\max} - \theta_{\min}) \times Def_{Fe} \quad (5c)$$

202 where $\theta_{\max}^{Fe}$ modulates θ by replacing $\theta_{\max}$. Together, these exacerbate the tendency for
203 light limitation under iron stress, representing co-limitation by iron and light. Note that

204 we chose linear dependencies in order to minimize complexity, rather than based on first
205 principles. The overall, light-limited photosynthesis rate is then calculated by equation
206 (1), in which I is the in-situ irradiance, except within the mixed layer where the irradiance
207 is vertically averaged in order to implicitly represent the turbulent transport of
208 phytoplankton throughout the mixed layer. Note that the irradiance used for calculating θ
209 and I_k (I_{mem}) is smoothed over one day to represent a small lag as phytoplankton adapt to
210 ambient light levels (Dusenberry et al., 2001).

211 Even with this small number of equations, the resulting interdependence on iron,
212 light, temperature, and macronutrient is significantly nonlinear. As illustrated in Figure 2,
213 the Geider (1997) formulation predicts that the total photosynthesis rate P^C increases as I
214 increases, but the response to I saturates more quickly when P_m^C is small (either because
215 of nutrient limitation or low temperature), since fewer photons are required to achieve the
216 slower light-saturated photosynthesis rates. This can be seen by inspection of equation 2,
217 in which the first term, $P_m^C / \alpha^{chl} \theta_{\max}^{Fe}$, gives the dependence of light limitation on
218 temperature and nutrient availability: when this term is large, more light is required to
219 approach light-saturated rates. Equation 2 also reveals that the iron dependencies of α^{chl}
220 and $\theta_{\max}^{Fe}$ carry more weight when P_m^C is large, and/or when the second term of equation 2
221 (I/2) is small. Thus, under low light, and at high temperatures, iron limitation has a larger
222 impact on the degree of light limitation. Meanwhile, at high PO_4 concentrations, Fe has a
223 very large impact on P_m^C through the Liebig limitation term, whereas when PO_4
224 concentrations limit P_m^C, iron limitation mainly acts through its effect on I_k.

225 Finally, combining our iron limitation scheme with the Geider et al. (1997)
226 formulation, we can diagnose a chlorophyll to carbon ratio

227 $$\theta = \frac{\theta_{\max}^{Fe}}{1 + \alpha^{chl}\theta_{\max}^{Fe} I_{mem} / 2P_m^C} \quad (11)$$

228 Increasing the iron concentration will thus affect θ via all three iron-dependent terms.
229 First, the increase of P_m^C will increase θ, as plankton manufacture chlorophyll in an
230 attempt to provide energy to achieve the higher light-saturated photosynthesis rate.
231 Second, the increase of $\theta_{\max}^{Fe}$ will cause θ to increase, with more impact at low light levels
232 than at high light levels. Third, an increase of α^{chl} will tend to *decrease* θ, particularly at
233 high light (since a given amount of chlorophyll becomes more efficient at processing
234 light). The net effect of iron addition on θ, as well as growth rate, is therefore dependent
235 on multiple environmental conditions.

236 The carbon-specific growth rate, μ, is equal to the photosynthesis rate minus
237 respiration. For simplicity, we follow Geider et al. (1997) in assuming that respiration is a
238 fixed fraction of the growth rate, and is thus incorporated into P^C for the experiments
239 described here, so that $\mu = P^C$ for the remainder of the discussion. All calculations are
240 made in terms of phosphorus, and are converted to carbon units assuming a constant C:P
241 of 106 and to oxygen units using an O_2:P of 150 (Anderson, 1995).
242
243 *b.) Mortality rate formulation*
244 The uptake of nutrients by phytoplankton depends on the carbon-specific growth
245 rate, multiplied by the biomass of living phytoplankton. The biomass, in turn, evolves
246 due to a small residual between total growth and total mortality rates. Many models keep
247 track of these terms explicitly, allowing direct calculation of mortality, but incorporating
248 additional computational expense. However, it is also possible to calculate the biomass

associated with a particular growth rate implicitly, circumventing the need for explicit biomass tracers, if we apply a simple mortality law.

Following the global observational synthesis of Dunne et al. (2005) we assume a mortality law of the form

$$Growth = \mu B = \lambda_T (B/P^*)^a B = Mortality \quad (6)$$

where B is the biomass in mol P kg^{-1}, λ_T is the temperature-dependent mortality rate (equivalent to the sum of all losses of living biomass through grazing, viral lysis, etc.) and P^* is a scaling term. The term a represents a mortality exponent, as discussed by Dunne et al. (2005). If a=1, the formulation corresponds to classic logistic growth, in which the mortality rate is linearly proportional to population density. If we assume that the temperature dependence of mortality is identical to that of growth such that $\lambda_T = \lambda e^{kT}$, the biomass B_x associated with the growth rate of a particular class of phytoplankton x is $B_x = (\mu_x / \lambda e^{kT})^{1/a_x} \times P^*$ so that the uptake rate of PO_4 is given as

$$V_{PO4_x} = (\mu_x / \lambda e^{kT})^{1/a_x} \times P^* \times \mu_x \quad (7)$$

Following most ecosystem models, we conceptualize the phytoplankton as including two subpopulations: 'large', which are consumed by mesozooplankton and are more likely to form more sinking particles, and 'small', which are consumed by microzooplankton and are more likely to decompose to dissolved and suspended organic matter. If we assume that small and large phytoplankton growth rates are the same under the same conditions (probably incorrect, but a useful simplifying assumption), $B_x = (\mu / \lambda e^{kT})^{1/a_x} \times P^*$. We follow Dunne et al. (2005) in using a = 1 for small phytoplankton (corresponding to an assumption that the rapidly reproducing

271 microzooplankton concentrations match small phytoplankton concentrations) and a = 1/3
272 for large phytoplankton.

273 This formulation produces a cubic relationship between large and small plankton,
274 consistent with the field data compilation of Agawin et al. (2000), and represents a
275 fundamental building block both of our model and of the more complex TOPAZ
276 biogeochemical model (Dunne et al., in prep.), used in the GFDL Earth System Model.
277 The total uptake is then

278 $$V_{PO4} = ((\mu / \lambda e^{kT})^3 + (\mu / \lambda e^{kT})) \times \mu \times P^* \quad (8)$$

279 Following Dunne et al. (2005) we use values of λ=0.19 day^{-1} e^{kT} and P*=1.9 μmol C kg^{-1}.

280 This key relationship allows us to diagnose a number of useful properties. For
281 example, the biomass is

282 $$B = ((\mu / \lambda e^{kT})^3 + (\mu / \lambda e^{kT}))P^* = B_{large} + B_{small} \quad (9)$$

283 Note that since the temperature dependence e^{kT} appears in both the numerator and
284 denominator of each term, the biomass itself is independent of temperature. From (9) the
285 fraction of biomass associated with large phytoplankton $frac_L$ is simply

286 $$frac_L = \frac{B_{large}}{B_{large} + B_{small}} = \frac{(\mu / \lambda e^{kT})^2}{1 + (\mu / \lambda e^{kT})^2} \quad (10)$$

287 such that at 0°C, if the growth rates exceed ~0.19 day^{-1}, large phytoplankton will be in
288 the majority, while at 28°C the growth rate must exceed 1.1 day^{-1} for this to be true.

289

290 *c.) Organic matter cycling*

291 Field observations show that nutrient elements are efficiently recycled within the
292 mixed layer, with a relatively small fraction being exported as dissolved or particulate

293 organic material (Dugdale and Goering, 1967). In order to model a realistic relationship
294 between gross primary production and export production, we must therefore represent the
295 division of nutrient uptake between recycling and export. Once again we follow the work
296 of Dunne et al. (2005) who examined 119 globally distributed sites at which the ratio
297 between particulate export and primary production (the pe-ratio) could be estimated from
298 observations. They developed a formulation that linked the pe-ratio to water column
299 remineralization, in terms of the production of detritus and ballasting material associated
300 with coccolithophorids and diatoms. As we do not explicitly represent sinking detritus,
301 we reanalyze the Dunne et al. (2005) dataset in terms of a simpler model of particle
302 sinking and remineralization.

303 As was recently noted by (Kriest and Oschlies, 2008) the classic "Martin curve"
304 profile for remineralization is consistent with a sinking speed that increases linearly with
305 depth and a remineralization rate that is constant. We chose a sinking speed of 16 m/day
306 over the top 80m, increasing linearly below that depth at a rate of 0.05(m/day)/m and an
307 oxygen-dependent remineralization rate with a maximum of γ_{DOP} of 0.12 day^{-1}. Figure
308 3a shows the resulting profile of particle flux, which lies between the classic Martin
309 curve of $F = F(z = 100m) \times (z/100)^{-0.868}$ and the function $F = F(z = 75m) \times (z/75)^{-0.9}$
310 used for the OCMIP2 simulations (see for example Gnanadesikan et al., 2002, 2004). The
311 remineralization rates (% primary production/m), shown in Figure 3b, are similar to the
312 previous parameterizations over most of the water column.

313 Following Dunne et al. (2005) we link large and small phytoplankton to a
314 remineralization scheme to derive a particle export ratio. We calculate values of ϕ_L and
315 ϕ_S, the detrital production fractions associated with large and small phytoplankton

316 respectively, to match the observational compilation in Dunne et al. (2005). The resulting
317 values of ϕ_L = 1.0 and ϕ_S =0.18 provide a fit that explains more than 60% of the variance
318 in the observations, as illustrated in Figure 3c, comparable to the fits found in Dunne et
319 al. (2005). The detritus production tends to be less than half the total uptake, and can be
320 as little as one tenth in warm, low-productivity waters. The non-detritus remainder is then
321 subdivided, such that a constant fraction ϕ_{DOP} is converted to dissolved organic
322 phosphorus, with the residual being instantaneously recycled to inorganic PO_4 to
323 represent the microbial loop (Figure 1). The magnitude of gross uptake (primary
324 production) is strongly dependent on this subdivision, but it has little effect on export
325 production. The remineralization of sinking detritus also produces both dissolved
326 inorganic and dissolved organic phosphorus, in the same ratio ϕ_{DOP}.
327
328 *d.) Iron cycling*
329 The iron cycle is inherently more complex than the phosphate cycle, primarily
330 because dissolved iron concentrations are more intensely modified by interactions with
331 particles than are dissolved phosphate concentrations (Parekh and Boyle, 2005). In an
332 oxygenated environment, iron (II) and (III) form colloids that are readily scavenged by
333 organic and mineral sinking particles, removing them from the water column (Wu et al.,
334 2001). On the other hand, iron can also be chelated by dissolved organic ligands, whose
335 concentrations can greatly exceed that of the iron itself, preventing the adsorption of iron
336 to particles (Rue and Bruland, 1995). Meanwhile, the uptake of chelated iron by plankton
337 (Tortell et al., 1999) and the photochemical breakdown of ligands (Barbeau et al., 2001)
338 can result in relatively short lifetimes for iron in the surface ocean (Weber et al., 2005;

339 Tagliabue and Arrigo, 2005). As a result of its high reactivity and rapid removal from the
340 ocean, the lifetime of iron in the ocean is much shorter than that of phosphate or nitrate,
341 resulting in a tight coupling of the iron distribution to its source regions (Johnson et al.,
342 1997). These sources include runoff (Hutchins et al., 1998), mineral dust (Mahowald et
343 al., 2003; Ginoux et al. 2004) and sediments (Lam et al., 2006; Moore and Braucher,
344 2008).

345 Given that the understanding of multiple forms of iron remains rudimentary, we
346 follow previous workers (e.g. Moore et al., 2004; Parekh et al., 2004; Aumont and Bopp,
347 2006) in defining a single pool of 'dissolved' iron. Iron is supplied to the ocean surface
348 layer according to a prescribed climatological aeolian dust source (Ginoux et al., 2004)
349 which totals 3.28 Gmol Fe a^{-1}. Iron is also supplied by diffusion from the seafloor,
350 representing the release of iron from organic and mineral phases in the sediment, as the
351 product of $Fe{:}P_{sed}$ and the sedimenting organic phosphorus flux, following Moore and
352 Braucher (2008). The sedimentary iron efflux varies with global export production, but is
353 on the order of 8 Gmol Fe a^{-1}.

354 We also include an implicit ligand, with a globally uniform concentration of 1 nM
355 following Parekh et al. (2005). We allow the ligand stability constant K_{FeL} to decrease
356 from $K_{FeL}^{\max}$ toward $K_{FeL}^{\min}$ in surface waters, which are diagnosed as a function of light
357 intensity I, inspired by the observed photodissociation of iron-ligand complexes in
358 surface waters (Barbeau et al., 2001, 2003):

359 $$K_{FeL} = K_{FeL}^{\max} - (K_{FeL}^{\max} - K_{FeL}^{\min}) * \frac{I^2}{I_{FeL}^2 + I^2} * \max(0,\min(1,\frac{Fe - Fe_{\min}}{Fe} * b)) \qquad (11)$$

360 where b is an arbitrary multiplier (equal to 1.2) to ensure that K_{FeL} approaches $K_{FeL}^{\max}$.
361 Since ligands and their reaction to light are not explicitly modeled, the light sensitivity

parameter, I_{FeL}, is set to a low value to maintain low values of K_{FeL} throughout the euphotic zone. The latter term in eq. 11 reduces photodissociation when iron concentrations Fe approach $Fe_{\min}$, to represent the formation of siderophores (strong ligands) by microbes under iron stress (Trick et al. 1983, Granger and Price, 1999). This results in a more rapid removal of iron from the surface ocean, a result that Moore and Braucher (2008) achieve instead by increasing the scavenging rate constant by roughly a factor of 6 in the upper ocean.

Free dissolved iron, i.e. not bound to the ligand, is scavenged by two mechanisms in oxic waters. The first, after Parekh et al. (2005), calculates a first-order scavenging rate constant as a function of the sinking flux of organic matter:

$$Fe_{ads}^{org} = k_{Fe}^{org} * (\frac{f_{POC}}{w})^{0.58} * Fe' \quad (12)$$

where the exponent of 0.58 is taken from the empirical study of Honeyman et al. (1988). Alone, this would ignore the unresolved effect of lithogenic material as a scavenging agent, as well as the inorganic formation of colloids. Therefore we include a second type of scavenging to represent these processes:

$$Fe_{ads}^{inorg} = k_{Fe}^{inorg} \times Fe'^{1.5} \quad (13)$$

Because the underlying processes are poorly understood, we use a globally uniform rate constant, and increase the order of the iron concentration dependence to represent the enhanced formation of colloids where iron concentrations are higher. Improving these parameterizations is a clear target for future work.

It is assumed that scavenged iron is released to the water column as it sinks; thus, adsorbed iron is returned to the dissolved pool following the same instantaneous sinking and remineralization routine applied to the particulate organic iron produced by

385 phytoplankton uptake. Particulate iron that sinks out of the bottom ocean layer is
386 permanently removed from the ocean, as long as oxygen concentrations are greater than
387 the anoxic threshold. Otherwise, the sedimented iron is instantaneously returned to the
388 bottom layer.
389
390 e.) *Parameter choices*
391 Parameter values (shown in Table 1) were initially selected based on a survey of
392 the available literature and/or first principles, and adjusted when necessary in order to
393 obtain a solution that compares reasonably well with observations. Note that the
394 parameter ranges for α^{chl} and $\theta_{\max}^{Fe}$ were set to provide identical responses to Def_{Fe}, rather
395 than as optimal fits to the data. The simulation was compared to the World Ocean Atlas
396 2001 and 2005, the dissolved iron compilation of Moore and Braucher (2008), the A16
397 section of Measures et al. (2008), and SeaWIFS satellite observations of chlorophyll
398 (Level 3 SeaWiFS chlorophyll-a concentration data, OC4, reprocessing v5.2, for
399 September 1997 - December 2007, downloaded from http://oceancolor.gsfc.nasa.gov/).
400 Note that the sedimentary iron efflux ratio was reduced significantly from its initial value,
401 in order to avoid overwhelming the relatively small atmospheric source.
402
403 f.) *Physical model*
404 The BLING model was embedded in the ocean component of the GFDL coarse-
405 resolution global coupled climate model, CM2Mc (Galbraith et al., in prep). This uses the
406 MOM4p1 code with pressure as the vertical coordinate, a free surface, 'real' freshwater
407 fluxes and a dynamic-thermodynamic sea ice module. The nominal resolution of this

408 model, OM1p7, is 3 degrees in the east-west direction, with resolution in the north-south
409 direction varying from 3 degrees in mid-latitudes to 2/3 degree near the equator.
410 Enhanced resolution is also applied at the latitudes of the Drake Passage as well as at the
411 symmetrically equivalent latitudes of the northern hemisphere. A tripolar grid is applied
412 to the Arctic, as in GFDL's CM2.0 and CM2.1 models (Griffies et al., 2005). The vertical
413 resolution is 28 levels, ranging from 10 m resolution at the surface to 506 m in the
414 lowermost layer. Tracer advection uses the Sweby MDFL scheme. The surface forcing is
415 a repeated climatological year derived from the Coordinated Ocean Reference
416 Experiment (Griffies et al., 2009), which also supplies shortwave irradiance to the ocean
417 (there is no diurnal cycle). Surface salinities are restored to observations with a time
418 constant of 10 days over the top layer. Light is absorbed by water and a smoothly-
419 varying, satellite-derived climatological chlorophyll field following the Manizza et al.
420 (2005) algorithm.

421 Subgridscale parameterizations for mixing are similar to those used in the CM2.1
422 series (Gnanadesikan et al., 2006). The lateral friction uses an isotropic Smagorinsky
423 viscosity in mid-latitudes, while within 20 degrees of the equator the anisotropic NCAR
424 viscosity is used, as in the CM2 series. Lateral diffusion of tracers along isopycnals is
425 subject to the thickness diffusion parameterization of Gent and McWilliams (1990) with a
426 spatially varying diffusion coefficient. The time scale in this coefficient depends on the
427 horizontal shear between 100m and 2000m while the spatial scale is constant. A
428 minimum coefficient of 500 m^2/s and a maximum coefficient of 1200 m^2/s are imposed.
429 The lateral diffusion coefficient for tracers is the same as the lateral diffusion coefficient
430 for thickness. The thickness transport saturates at a value $A_I * S_{max}$ where S_{max} is set to

0.02 (see Gnanadesikan et al., 2007 for discussion of potential impacts of this parameter). Within the mixed layer, we use the K-profile parameterization of Large et al., (1993). Away from the mixed layer, a background diffusivity of 0.1×10^{-4} m^2 s^{-1} and a background viscosity of 1×10^{-4} m^2 s^{-1} is used. Below 500m, these background coefficients are enhanced by using the scheme of Simmons et al. (2004) to parameterize a tidally-dependent mixing that depends on the in situ stratification as well as prescribed bottom roughness and tidal amplitude.

g.) *Model simulations*

Because the performance of the biogeochemical model intimately depends on the physical model in which it is embedded, we refer to the coupled ocean-biogeochemical model here as BLING-om1p7. Initial conditions for ocean temperature and salinity were interpolated from the World Ocean Atlas 2001 to the model grid, and the model was started from rest. Phosphate and oxygen concentrations were taken from the World Ocean Atlas 2005. Iron was initialized from a constant global value of 0.6 nM and integrated for 200 years with a preliminary version of the model, to prevent large drift upon initialization. The model was then spun up for 400 years with the AllVar configuration (see below), allowing for the iron cycle and the nutrient structure of the thermocline to come to near equilibrium. Over the final century RMS changes in surface phosphate were less than 0.01 μM in this run, indicating that we have reached a relatively steady state at the surface. A suite of eight experiments was then initialized from this spun-up state, and each was integrated for 100 years. These form the basis of the discussion in part 3. In all cases, the final year of each run was analyzed.

454 We describe here the global simulation of the model experiment that includes all
455 three iron limitation terms (which we refer to below as AllVar). The model simulates
456 surface macronutrient concentrations with reasonable fidelity. Note that, although
457 nitrogen is the more important limiting macronutrient in the ocean, we refer to our
458 limiting macronutrient as 'PO_4', because we do not include denitrification and nitrogen
459 fixation. We therefore compare our modeled PO_4 to an "average macronutrient" equal to
460 (phosphate+nitrate/16)/2. The last column in Table 2 shows correlation and regression
461 coefficients between the modeled macronutrient and the average macronutrient in this
462 simulation. Correlation and regression coefficients all exceed 0.87, and the overall
463 patterns of surface macronutrients are generally realistic (Figure 4a,b). The annual
464 standard deviation of nutrient concentrations (Figure 4c,d) exhibits a large-scale
465 similarity between modeled concentration and observations, with small ranges in the
466 subtropical gyres and larger ranges along the equator, in the Southern Ocean and in
467 northern subpolar gyres. The data (Figure 4d) has a lot of small-scale variability, much of
468 which may result from undersampling and interpolation; in addition, when biases in the
469 physical circulation are considered, the correlation of 0.58 is not unreasonable.
470 As seen in Figure 5, this experiment also reproduces the contrast between low-
471 chlorophyll gyre centers and the higher chlorophyll upwelling zones and subpolar
472 regions, as seen in satellite observations. The regression coefficient for the log
473 chlorophyll concentration is 0.86, while the correlation coefficient is 0.90. The low value
474 of the regression coefficient is likely related to the inability of BLING-om1p7 to
475 reproduce intense blooms in coastal regions.

476 The simulated surface concentration of iron (Figure 6a) range from high values
477 (exceeding 1.5 nM) in coastal regions, with relatively high values of 0.8-1.0 nM in the
478 dust deposition plumes of the Atlantic and Northern Indian Oceans, similar to the data
479 compilation of Moore and Braucher (2008). Significant seasonal cycles (Figure 6b) occur
480 over much of the world ocean, with large variations beneath dust plumes, in convective
481 regions and in the western parts of subtropical gyres. These seasonal cycles are due to
482 resupply of iron during deep mixing, removal of iron by sinking particulate organic
483 matter during the growth season, and the seasonal cycle of iron deposition, and likely
484 contribute to small-scale variability in the observational database (Figure 6a). Measures
485 et al. (2008) recently published a high-resolution section of iron along the A16N track.
486 Figure 6c shows that the model produces a very similar spatial structure with low values
487 in the surface North Atlantic and immediately south of the Equator, with higher values at
488 depth and a plume of high iron north of the equator, centered around 15°N. Our values
489 are somewhat lower than observed, particularly beneath the Saharan plume, but otherwise
490 the agreement is encouraging given the many uncertainties in the source and sink terms
491 for iron. The response of photosynthesis to spatial variations of dissolved iron is given
492 by the term Def_{Fe} in the model, presented in equation (4). As shown in Figure 6d, Def_{Fe} is
493 near 1 (no limitation) close to shallow sediments, and near deserts where dust deposition
494 is high. In the northern subpolar gyres it ranges between values of 0.4 and 0.6 while in
495 the equatorial Pacific and Southern Ocean values of 0.1-0.3 are found. Iron limitation
496 thus introduces spatial asymmetries between the hemispheres, as well as between the
497 equatorial Atlantic and Pacific Oceans.

Following Gnanadesikan et al. (2004) and Dunne et al. (2007) we compare our model output with three satellite-based primary productivity estimates, developed by Behrenfeld and Falkowski (1997), Carr (2002) and Marra et al. (2003). As seen in Figure 7a, the Carr (2002) algorithm closely matches the overall production (61 GtC vs 63.4 GtC/yr) and time-varying pattern (correlation of 0.75). The modeled export diverges somewhat more from the observations (Figure 7b), being overly dominated by high productivity regions, the physical representation of which may be poorly resolved in our coarse model. Additionally, our model tends to concentrate production and export in subpolar regions during the strong spring bloom, while the satellite-based estimates show more productivity during summertime months.

3. Deconstructing the global response to aspects of iron limitation

BLING simulates global spatial and temporal variability of dissolved Fe concentrations throughout the ocean, which are then used to calculate Def_{Fe}. We explore the global biogeochemical response to physiological representations of iron limitation by starting with a version of the model in which the simulated iron concentrations have no effect on photosynthesis, and subsequently introduce an iron dependency to each of the three terms α^{chl}, $\theta^{Fe}_{\max}$ and P^{C}_{m}, both alone and in combination. A model that ignores the effect of iron limitation on any one of the three relevant terms would use something close to the mean value for each, rather than removing the term altogether; we therefore 'eliminate' the effect of iron by replacing Def_{Fe} with the global mean value. This means that including the effect of iron will cause growth rates to increase in iron-rich regions, and to decrease in iron-poor regions, all else remaining equal. We refer to the run in

521 which the simulated iron has no effect on growth as AllMean, and the run in which all
522 three terms depend on the simulated iron as AllVar (note this is the configuration
523 described in section 2g, above). The mean Def_{Fe} is determined from the final century of
524 the AllVar run (equal to 0.4595). Intermediate between AllMean and AllVar are Varα,
525 Varθ and VarLiebig, in which iron affects only one of α^{chl}, $\theta_{\max}^{Fe}$ and P_m^C, respectively,
526 and Varα+θ, Varθ+Liebig and Varα+Liebig, in which all but one of the three parameters
527 depends on the simulated iron concentrations. It is important to recognize that α^{chl} and
528 $\theta_{\max}^{Fe}$ have numerically identical effects on I_k in our formulation (and given our parameter
529 choices), such that their product essentially represents the efficiency with which incident
530 light is harvested by the phytoplankton. Hence, we present the results for the two as
531 interchangeable (with the exception of their impacts on chlorophyll, which differ).
532 The lower panels of Figure 7 show the global impact of including iron
533 dependencies on primary production and export production. Unsurprisingly, the
534 interhemispheric asymmetry in iron supply causes primary productivity to decrease in the
535 iron-poor southern hemisphere, and to increase in the northern hemisphere, for all iron
536 limited runs, relative to AllMean (Figure 7c). All iron-dependent runs also show a slight
537 decrease in primary productivity on the equator, though more pronounced is a meridional
538 widening of the high-productivity zone. Meanwhile, changes in particle export follow a
539 similar pattern but show extreme differences in the Southern Ocean – though striking,
540 this simply follows from the nonlinear increases of biomass and particle export with
541 increasing growth rates. However, a surprising response is evidenced in the relative
542 sensitivities of different iron limitation terms. In the northern hemisphere, the subsequent
543 inclusion of each additional iron dependency causes the export to increase, such that each

544 term appears to be of roughly equivalent importance. In contrast, within the Southern
545 Hemisphere, the inclusion of the light-harvesting efficiency terms (Varα and Varθ) only
546 have an impact when VarLiebig is not included. All simulations including an iron-
547 dependent light-saturated growth rate (VarLiebig, Varθ/α+Liebig and AllVar) are nearly
548 indistinguishable. This begs the question, why does an iron dependency in the light-
549 saturated growth rate (VarLiebig) overwhelm the iron dependency of the light harvesting
550 efficiency (Varα and Varθ), and why is this so pronounced in the Southern Ocean?
551 To understand the results of the experiments we undertake a more detailed
552 analysis, beginning with the impact of variable iron limitation on the surface PO_4 field.
553 As shown in Figure 8b, the AllMean simulation greatly underestimates surface PO_4,
554 relative to observations, in the Southern Ocean, eastern equatorial Pacific, and subarctic
555 Pacific. Including an iron dependency in any of the three photosynthesis terms, in any
556 combination, reduces the total error relative to observations (see also Table 2). However,
557 the strongest effect is clearly associated with the light-saturated photosynthesis term,
558 VarLiebig (Figure 8d,f,h), which greatly outweighs the significance of the other terms –
559 again, particularly in the Southern Ocean, as shown in the zonal mean (Figure 7). This
560 suggests that either our formulation has placed too much weight behind the VarLiebig
561 term, or that the net result of including multiple limitations tends to largely eliminate the
562 impacts of photosynthetic efficiency on the surface nutrient field.
563 The photosynthetic efficiency terms (Varα and Varθ) do have a significant impact
564 on light limitation (Figure 9), as expected, causing changes that are of approximately the
565 same magnitude as those of VarLiebig (Figures 9b vs. 9c). However, they are dominantly
566 of the opposite *sign* of the VarLiebig changes. In the VarLiebig case (Figure 9d), the

reduction of P_m^C within iron-limited domains actually causes a decrease in the severity of light limitation (e.g. in the Southern Ocean). Thus, if the ability to synthesize chlorophyll and photosynthetic reaction centers is unaffected by iron concentrations, the sole effect of iron limitation is to decrease the light-saturated photosynthesis rate P_m^C, thereby decreasing the demand for light. In contrast, including iron dependencies in only the photosynthetic efficiency terms (experiments Varα/θ and Varα+θ) clearly exacerbates light limitation in regions with low Def_{Fe}, more consistent with observations (Maldonado et al., 1999; Hiscock et al., 2008).

Nonetheless, in the global simulation, the effects of iron on photosynthetic efficiency and the effects of iron on the total growth rate (Figure 10) look very different. First, in the Southern Ocean, the impact of photosynthetic efficiency on light limitation is clearly significant when it acts alone, decreasing the light limitation term by up to ~25% (Figure 9, panels b and d). However, the importance of photosynthetic efficiency on the Southern Ocean is almost entirely muted when the light-saturated growth rate is also affected by iron (Figure 10, panels e and g). This is because the light limitation term of eq. (2), $P_m^C / \alpha^{chl} \theta_{\max}^{Fe}$, becomes vanishingly small as iron becomes very limiting in the Liebig component of P_m^C, an effect that is further exaggerated due to the low temperatures of the Southern Ocean (making P_m^C even smaller). Thus, the tendency for photosynthetic efficiency to deteriorate under extreme iron limitation is ameliorated by the low energy demand at the very low inherent growth rates. In contrast, in relatively warm waters where iron is abundant, the light limitation term $P_m^C / \alpha^{chl} \theta_{\max}^{Fe}$ is relatively large, providing increased leverage to variability of α^{chl} and $\theta_{\max}^{Fe}$ and thereby

accentuating iron-light colimitation. This is evident in the enhanced light limitation in the tropical Pacific, off equator, which persists when VarLiebig is included (Figure 9, panels b and d vs. e and g). In physiological terms, the inherent ability of phytoplankton to grow more quickly in warm waters gives them a greater demand for usable electrons, and therefore makes them more dependent on efficient photosynthetic machinery. We point out that this prediction arises directly from our theoretically-based inclusion of iron limitation in the Geider photoadaptation framework; its relevance should be tested by field and laboratory experiments.

However, despite the fact that the tropical Pacific becomes much more light limited when photosynthetic efficiency depends on iron concentrations, this region actually experiences an increase in growth rates in these same simulations (Figure 10b,d). This occurs because overall growth rates are not just a function of light limitation but also of nutrient availability, which is modulated by ocean circulation and nutrient cycling, presenting non-local effects. In the tropical Pacific (off-equator), the supply of PO_4 to this otherwise P-starved region is increased by greater leakage from the equatorial Pacific, as the latter region becomes more iron limited (compare Figures 9b,d, 10b,d). Essentially, the increase of maconutrient abundance in this region, caused by iron limitation upstream, more than compensates for the enhanced light limitation in the simulations.

These nuances help to explain the finding, pointed out in Figure 7, that the effect of iron on photosynthetic efficiency is almost completely overwhelmed by that of the Liebig term, outside of the northern oceans. In these regions, greater iron availability allows phytoplankton to grow more quickly, making them more hungry for light and therefore more sensitive to the photosynthetic efficiency terms, as revealed by the

responses to Varα and Varθ. Meanwhile, near tropical upwellings, decreases in photosynthetic efficiency are counterbalanced by large increases in macronutrient supply, which end up dominating changes in growth rate. Finally, in the Southern Ocean, when phytoplankton are limited by low temperatures and low iron, the resulting low growth rates mean that the plankton do not need a lot of light, and thus show little additional response to Varα and Varθ. This leads to the remarkable paradox that when iron is most scarce, its effect on photosynthetic efficiency has the least impact on biogeochemistry.

Importantly, the greater impact of photosynthetic efficiency on production in the northern hemisphere (Figure 7) is not due to an overall increase in annually averaged growth rates (compare panels 10c and 10f). Instead, it acts through modulation of the seasonal cycle. As shown in Figure 11a, the annual cycle of productivity in the North Atlantic (70°W-0°,50°N-65°N) reveals distinct impacts from all three limitation terms. All contribute to intensifying the spring bloom and shifting it earlier, due to the relative abundance of iron resupplied from below by deep winter mixing, and to suppressing production during summer, due to more rapid nutrient depletion. Because of the strong degree of nonlinearity between growth and export, a more intense spring bloom produces a much higher annually integrated particle export. Surface chlorophyll (Figure 11b) shows a similar pattern, with the exception that increased growth rates in experiments including Varα are compensated by a lower chl:C ratio, so that α^{chl} has little impact on chlorophyll. In contrast, in the Southern Ocean (80°S-50°S), the inclusion of regionally dependent iron limitation suppresses growth rates, and prevents strong blooms. Inclusion of an iron dependency on the maximum light-saturated photosynthesis rate, in experiment Var Liebig (red line), has a large impact on the seasonal cycle, so that Varα+Liebig,

635 Varθ+Liebig (light blue line) and AllVar (dashed black line) are essentially identical to
636 VarLiebig. As discussed above, this reflects the relatively low utility of light to cells with
637 low maximum photosynthesis rates, arising from the cold waters and perennial iron-
638 limitation of P_m^C, so that photosynthetic efficiency has little role to play. Surface
639 chlorophyll (Figure 11d) shows more of a temporal impact as iron deficiency is added,
640 with the more iron-limited cases showing a dip in chlorophyll as iron limitation impedes
641 chlorophyll synthesis during the very iron-depleted summer.
642
643 **4. Conclusions**
644 We have developed a simplified model of oceanic biogeochemical cycling built
645 upon the photoadaptation model of Geider et al. (1997) and the biogeochemical
646 algorithms of particle export developed by Dunne et al. (2005). The resulting model,
647 BLING, simulates phytoplankton growth rates from instantaneous macronutrient and
648 micronutrient concentrations, temperature, and light limitation. Then, through a
649 parameterization of ecosystem processes, BLING uses those growth rates in order to
650 determine biomass, uptake, dissolved organic matter production and the export of sinking
651 particles. Embedded in a general circulation model of the ocean, BLING reproduces
652 many features of the large-scale nutrient and chlorophyll fields, but because it uses
653 relatively few prognostic tracers it can be run relatively cheaply.
654 We used this model to explore the impacts of variously applying iron
655 dependencies to the light-saturated photosynthesis rate (P_m^C), the efficiency with which
656 each unit of chlorophyll produces usable electrons at low levels of light (α^{chl}), and the
657 ability of the plankton to synthesize chlorophyll, $\theta_{\max}^{Fe}$. In general, including iron-

dependent photosynthesis terms reduced growth rates in macronutrient-rich regions (primarily the Southern Ocean, equatorial Pacific, and subarctic Pacific) and allowed macronutrients to leak to neighbouring oligotrophic regions, increasing growth rates there (Figure 10f). Including an iron dependency of P_m^C (experiments with VarLiebig) had the largest effect on all aspects of the simulation. This included a remarkably large effect on light limitation, since iron limitation decreases P_m^C, reducing the degree of light limitation by shrinking the first term of eq. (2), $P_m^C / \alpha^{chl} \theta_{\max}^{Fe}$, and thereby mitigating iron-light colimitation. In physiological terms, this represents a reduction in the usefulness of light to a phytoplankton community whose light-saturated growth rates are severely restricted by a lack of Fe, even when the ability to harvest light is itself hampered by iron-limited decreases of α^{chl} and/or $\theta_{\max}^{Fe}$. This general tendency seems to be supported by at least one laboratory experiment, carried out with a *Chaetoceros* diatom (Davey and Geider, 2001), for which changes in chlorophyll-normalized P_m^C (i.e. P_m^B) under varying iron limitation were of approximately the same magnitude as α^{chl}, so that $P_m^C / \alpha^{chl} \theta_{\max}^{Fe}$ remained approximately constant. In contrast, where P_m^C increases as a result of abundant iron and/or PO_4, the importance of iron dependencies on α^{chl} and $\theta_{\max}^{Fe}$ also increase, since the term $P_m^C / \alpha^{chl} \theta_{\max}^{Fe}$ becomes relatively large. Temperature has a related effect on light limitation in the simulations, since at high temperature, rapid light-saturated photosynthesis rates increase the demand for light, leading to a greater importance of iron-light colimitation in tropical waters. In contrast, the low inherent growth rates in cold waters of the Southern Ocean reduced the demand for photons, such that the impact of iron on photosynthetic efficiency was relatively unimportant.

Figure 12 illustrates the effect of this interaction between terms on the export production, with panel (a) showing the linear sum of the changes in export production expected from experiments Varα/θ and VarLiebig, and panel (b) showing the changes in export production actually simulated in experiment AllVar. The difference between these two panels reveals the impact of VarLiebig on the impact of the photosynthetic efficiency. In most of the world, the impact of iron on photosynthetic efficiency is muted by the effect on P_m^C. Only in parts of the northern hemisphere, where high seasonal abundances of iron drive all three terms to increase, does the amplitude of change in the AllVar model exceed the linear sum. We would emphasize that the degree to which these predictions hold depends on the details of our formulation and choice of parameters – the model presented here is certainly wrong in many respects. Nonetheless, these clear predictions offer a target that iron enrichment experiments can test by deliberately isolating the effects of temperature, macronutrient limitation, and light.

The correlation and regression coefficients for the range of experiments (Table 2) showed little improvement when Varα was included, for which we offer an explanation here. Much of the conceptual basis for this paper is based on pulsed iron additions applied to bottle incubations or mesoscale patches, which reflect the response of a given species or community to changes in iron availability. However, observations of natural communities across gradients of iron availability in the Southern Ocean suggest that community-wide responses to long-term iron limitation may diverge from the more clear-cut, short-term responses of iron-fertilization experiments. In particular, Hopkinson et al. (2007) showed that changes in α^{chl} between naturally iron-rich shelf and iron-poor open-ocean waters had no clear relationship to iron availability.

We propose that the long-term adjustment of ocean ecosystems to the available iron supply differs from the short-term response of biota to pulsed iron enrichments, in terms of α^{chl}. The tendency for communities to become dominated by small plankton under iron-limitation, simply due to diffusion effects (Morel et al., 1991), will serendipitously increase α^{chl}, since small plankton have inherently more efficient photosynthetic machinery due to reduced 'packaging effects' (Greene et al., 1991). Thus, we speculate that even though many phytoplankton (particularly diatoms) can increase their photosynthetic efficiencies given sufficient iron (Strzepek and Harrison, 2004), the phytoplankton that dominate iron-limited systems have inherently high photosynthetic efficiencies, so that the global distribution of iron is not strongly correlated with α^{chl}. The fact that our experiments show clear improvements in the simulations of global macronutrients (Table 2) when both P_m^C and θ vary (experiment Varθ+Liebig), but not when α^{chl} is allowed to vary as well (experiment AllVar), would be consistent with a weak dependence of α^{chl} on iron across natural communities.

In closing, our results suggest that models which do not parameterize the effects of iron availability on photosynthetic efficiency are not missing much in terms of simulating global-scale biogeochemistry, due to the dominant impact of iron availability on the light-saturated photosynthesis rate. However, they are likely to impact more subtle features of global simulations, such as the distribution of chlorophyll, and the seasonal cycle of primary production, particularly spring blooms in the North Atlantic.

Acknowledgements

We thank Stephanie Henson for providing the SeaWifs climatology, and Christopher Measures for sharing the iron concentration data. Adrian Marchetti and Julie Granger commented on an early version of the draft. We thank Charlie Stock for useful discussions.

730 **References**

731 Agawin, N. S. R., Duarte, C.M, and Agusti,S.: Nutrient and temperature control of the
732 contribution of picoplankton to phytoplankton biomass and production, Limnol.
733 Oceanogr., 45, 591– 600.
734 Anderson, L.A : On the hydrogen and oxygen content of marin phytoplankton. Deep Sea
735 Res. Pt. I, 42, 1675-1680,1995.
736 Aumont, O. and Bopp, L.: Globalizing results from in-situ iron fertilization studies,
737 Global Biogeochem. Cy., 20, GB2017, doi:10.1029/2005GB002591, 2006.
738 Barbeau, K., Rue, E.L, Bruland, K.W., and Butler,A.: Photochemical cycling of iron in
739 the surface ocean mediated by microbial iron(III)-binding ligands. Nature 413: 409-
740 413, 2001.
741 Barbeau, K., Rue, E.L. Trick. C.L., Bruland, K.W. and Butler,A.: Photochemical
742 reactivity of siderophores produced by marine heterotrophic bacteria and
743 cyanobacteria based on Fe(III), Limnol Oceanogr., 48, 1069-1078, 2003.
744 Behrenfeld, M. J., and Falkowski, P.G.: Photosynthetic rates derived from satellite-based
745 chlorophyll concentration, Limnol. Oceanogr., 42, 1 –20, 1997.
746 Behrenfeld, M.J., Boss, E., Siegel, D.A. and Shea, D.M.: Carbon-based ocean
747 productivity and phytoplankton physiology from space, Global Biogeochemical Cy.,
748 GB10006, doi:10.1029/2004GB002299, 2005.
749 Boss, E. and coauthors: Observations of pigment and particle distributions in the western
750 North Atlantic from an autonomous float and ocean color satellite, Limnol.
751 Oceanogr., 53, 2112-2122, 2008.

752 Boyd, P.W. and coauthors: The evolution and termination of an iron-induced mesoscale
753 bloom in the northeastern subarctic Pacific, Limnol. Oceanogr., 50, 1872-1886, 2005.
754 Boyd, P.W. and coauthors: Mesoscale iron enrichment experiments 1993-2005: Synthesis
755 and future directions, Science, 315, 612 – 617, 2007.
756 Carr, M.-E.: Estimation of potential productivity in Eastern Boundary Currents using
757 remote sensing, Deep Sea Res., Part II, 49, 59–80, 2002.
758 Davey, M. and Geider, R.J.: Impact of iron limitation on the photosynthetic apparatus of
759 the diatom *Chaetoceros muelleri* (bacillariophyceae), J. Phycol., 37, 987-1000, 2001.
760 Doney, S.C., Lindsay, K., Fung,I. and John, J.: Natural variability in a stable, 1000- Yr
761 global coupled carbon-climate model simulation, J. Climate, 19, 3033-3054, 2006.
762 Dugdale, R.C. and Goering, J.J.: Uptake of new and regenerated forms of nitrogen in
763 primary productivity, Limnol. Oceanogr., 12, 196-206, 1967.
764 Dunne, J.P., Armstrong, R.A., Gnanadesikan,A. and Sarmiento, J.L.: Empirical and
765 mechanistic models of the particle export ratio, Global Biogeochemical Cycles, 19,
766 GB4026, doi:10.1029/2004GB002390, 2005.
767 Dunne, J. P., Sarmiento, J.L. and Gnanadesikan, A.: A synthesis of global particle export
768 from the surface ocean and cycling through the ocean interior and on the seafloor.
769 Global Biogeochemical Cycles, 21, GB4006, doi:10.1029/2006GB002907, 2007.
770 Dusenberry, J., Olson, R.J. and Chisholm, S.W.: Photoacclimation kinetics of single-
771 celled fluorescence in laboratory and field populations of Prochlorococcus, *Deep Sea*
772 *Res. I*, 48, 1443-1458,2001.

773 Dutkiewicz, S., Follows,M.J. and Parekh, P.: Interactions of the iron and phosphorus
774 cycles: A three-dimensional model study, Global Biogeochemical Cy., 19, GB1021,
775 doi:10.1029/2004GB002342, 2005.
776 Eppley, R. W.: Temperature and phytoplankton growth in the sea, Fish. Bull., 70, 1063-
777 1085, 1972.
778 Frennette, J.J., Demers, S., Legendre, L. and Dodson, J.: Lack of agreement among
779 models for estimating the photosynthetic parameters, Limnol. Oceanogr., 38, 679-
780 687, 1993.
781 Geider, R.J., MacIntyre, H.L. and Kana,T.M.: Dynamic model of phytoplankton growth
782 and acclimation: Response of the balanced growth rate and chlorophyll a to carbon
783 ratio to light, nutrient limitation and temperature, Mar. Ecol. Prog. Ser., 148, 187-201,
784 1997.
785 Gent. P.J. and McWilliams, J.C.: Isopycnal mixing in ocean circulation models, J. Phys.
786 Oceanogr.,20, 150-155.1990.
787 Ginoux, P., Prospero, J.M., Torres, O., and M. Chin, M.: Long-term simulation of global
788 dust distribution with the GOCART model: correlation with North Atlantic
789 Oscillation, Environmental Modelling and Software, 19, 113-128, 2004.
790 Gnanadesikan A., and co-authors: GFDL's CM2 Global Coupled Climate Models- Part 2:
791 The baseline ocean simulation, J.Climate, 19, 675-697, 2006.
792 Gnanadesikan, A., Dunne, J.P., Key, R.M., Matsumoto, K., Sarmiento, J.L., Slater, R.D.
793 and Swathi , P.S.: Oceanic ventilation and biogeochemical cycling: Understanding
794 the physical mechanisms that produce realistic distributions of tracers and

productivity. Global Biogeochemical Cycles, 18(4), GB4010, doi:10.1029/2003GB002097, 2004.

Gnanadesikan, A, Slater, R.D., Gruber,N. and Sarmiento, J.L.: Oceanic vertical exchange and new production, a comparison between models and data, Deep Sea Res. Pt. II, 49, 363-401, 2002.

Gnanadesikan, A., Griffies, S.M., and B.L. Samuels, B.L.: Effects in a climate model of slope tapering on neutral physics schemes, *Ocean Modelling*, 16, 1-16, doi:10.1016/j.ocemod.2006.06.004, 2007.

Granger, J. and Price, N.M.: The importance of siderophores in the iron nutrition of heterotrophic marine bacteria, Limnol. Oceanogr., 44, 541-555, 1999.

Greene, R.M., Geider, R.J., and Falkowski, P.G: Effect of iron limitation on photosynthesis in a marine diatom, Limnol. Oceanogr., 36, 1772-1782, 1991.

Griffies, S.M. and coauthors: Coordinated Ocean-ice Reference Experiments (COREs), Ocean Modelling, 26, 1-46, 2009.

Griffies, S.M. Gnanadesikan, A., Dixon, K.W., Dunne, J.P., Gerdes, R.. Harrison, M.J., Rosati, A., Russell, J. L., Samuels, B. L., Spelman, M.J., Winton, M. and Zhang, R. 2005: Formulation of an ocean model for global climate simulations. Ocean Science, 1, 45-79, 2005.

Hiscock, M.R., Lance, V.P., Apprill, A, Bidigare, R.R, Johnson, Z.I., Mitchell, B.G. Smith, W.O., andBarber, R.T.: Photosynthetic maximum quantum yield increases are an essential component of the Southern Ocean phytoplankton response to iron, Proc. Natl. Acad. Sci., 105, 4775-4780, 2008.

817 Honeyman, B., Balistrieri, L. and Murray, J.: Oceanic trace metal scavenging and the
818 importance of particle concentration, Deep Sea Res., Pt I, 35, 227-246, 1988.
819 Hopkinson, B.M., Mitchell, B.G. Reynolds, R.A., Wang, H., Selph, K.E., Measures,
820 C.I., Hewes, C.D., Holm-Hansen, O., and Barbeau, K.A.: Iron limitation across
821 chlorophyll gradients in the southern Drake Passage: Phytoplankton responses to iron
822 addition and photosynthetic indicators of iron stress. Limnol. Oceanogr., 52(6), 2540-
823 2554, 2007.
824 Hutchins, D.A., DiTullio, G.R., Zhang, Y. and Bruland, K.W.: An iron limitation mosaic
825 in the California upwelling regime, Limnol. Oceanogr. 43, 1037-1054, 1998.
826 Johnson, K., Gordon, R.M. and Coale, K.H.: What controls dissolved iron concentrations
827 in the world ocean? Mar. Chem., 57, 137-161, 1997.
828 Kriest, I. and Oschlies, A. : On the treatment of particulate organic matter sinking in
829 large-scale models of marine biogeochemical cycles, Biogeosciences, 5, 55-72, 2008.
830 Lam, P. J., Bishop, J. K. B. , Henning, C. C. , Marcus, M. A. , Waychunas, G. A. and
831 Fung, I.Y.: Wintertime phytoplankton bloom in the subarctic Pacific supported by
832 continental margin iron, Global Biogeochem. Cycles, 20, GB1006,
833 doi:10.1029/2005GB002557, 2006.
834 Large, W., McWilliams, J.C., and Doney, S.C.: Oceanic vertical mixing: A review and a
835 model with a nonlocal boundary mixing parameterization. Rev. Geophys., 32, 363–
836 403, 1994.
837 Mahowald, N. M., Baker, A.R., Bergametti, G., Brooks, N., Duce, R.A., Jickells, T.D.,
838 Kubilay, N., Prospero, J.M. and I. Tegen, I.: Atmospheric global dust cycle and iron

839 inputs to the ocean, Global Biogeochem. Cycles, 19, GB4025,
840 doi:10.1029/2004GB002402, 2005.
841 Maldonado, M.T. , Boyd, P.W., Harrison, P.J., and Price, N.M.: Co-limitation of
842 phytoplankton growth by light and Fe during winter in the NE subarctic Pacific
843 Ocean, Deep-Sea Research II, 46, 2475-2485, 1999.
844 Manizza, M., Le Quere, C. Watson, A. J. and Buitenhuis, E.T.: Bio-optical feedbacks
845 among phytoplankton, upper ocean physics and sea-ice in a global coupled model,
846 Geophysical Research Letters, 32, L05603, doi:10.1029/2004GL020778., 2005.
847 Marchetti, A.,Juneau, P., Whitney, F.A., Wong, C.S. and Harrison, P.J., Phytoplankton
848 processes during a mesoscale iron enrichment in the NE subarctic Pacific: Part III-
849 primary productivity, Deep Sea Res. II, 53, 2131-2151, 2006a.
850 Marchetti, A., Maldonado, M.T.,Lane, E.S., Harrison, P.J.: Iron requirements of the
851 pennate diatom Pseudo-nitzschia: Comparison of oceanic (high-nitrate, low-
852 chlorophyll waters) and coastal species, Limnol. Oceanogr., 51, 2092-2101, 2006b.
853 Marchetti, A. and Harrison, P.J.:, Coupled changes in the cell morphology and the
854 elemental (C,N, and Si) composition of the pennate diatom Pseudo-nitzaschia due to
855 iron deficiency, Limnol. Oceanogr., 52(5), 2270-2284, 2007.
856 Marchetti, A., Parker, M.S., Moccia, L.P., Lin, E.O., Arrieta, A.L., Ribalet, F., Murphy,
857 M.E.P., Maldonado, M.T., and Armbrust, E.V.: Ferritin is used for iron storage in
858 bloom-forming marine pinnate diatoms, Nature, 457, 467-470, 2009.
859 Marra, J., Ho, C., and Trees, C.C.: An alternative algorithm for the calculation of
860 primary productivity from remote sensing data, LDEO Tech. Rep. LDEO-2003-1,
861 Lamont Doherty Earth Obs., Palisades, N. Y, 2003.

862 Measures, C.I., Landing, W.M. , Brown M.T., and Buck, C.S.: High resolution Al and Fe
863 data from the Atlantic Ocean CLIVAR-CO2 Repeat Hydrography A16N transect:
864 Extensive linkages between atmospheric dust and upper ocean geochemistry, Global
865 Biogeochem. Cycles, 22, GB1005, doi:10:1029/2007GB003042, 2008.
866 Milligan, A. J. and Harrison, P. J: Effects of non-steady-state iron limitation on nitrogen
867 assimilatory enzymes in the marine diatom Thalassiosira weissflogii
868 (bacillariophyceae), J. Phycol. 36, 78-86, 2000.
869 Moore, J.K., Doney, S.C., and K. Lindsay, K.: Upper ocean ecosystem dynamics and iron
870 cycling in a global 3-D model, Global Biogeochem. Cycles, 18, GB4028,
871 doi:10.1029/2004GB002220, 2004.
872 Moore, J.K. and Braucher, O.: Sedimentary and mineral dust sources of dissolved iron to
873 the world ocean, Biogeosciences, 5, 631-656, 2008.
874 Morel, F.M.M., Hudson, R.J.M., and Price, N.M.: Limitation of productivity by trace
875 metals in the sea, Limnol. Oceanogr., 36, 1742-1755, 1991.
876 Najjar, R.G. and Orr, J.C.: Biotic HOWTO, Internal OCMIP Report, LSCE/CEA Saclay,
877 Gif-sur-Yvette, France, 15pp., 1999.
878 Parekh, P.,Follows, M.J., and Boyle, E.A.: Decoupling of iron and phosphate in the
879 global ocean, Global Biogeochem. Cy., 19, GB2020, 10.1029/2004GB002280, 2005.
880 Price, N.M., Andersen, L.F., and Morel, F.M.M.: Iron and nitrogen limitation of
881 equatorial Pacific plankton, Deep Sea Res. I, 38, 1361-1378, 1991.
882 Raven, J.: Predictions of Mn and Fe use efficiencies of phototropic growth as a function
883 of light availability for growth and of C assimilation pathway, New Phytol., 116,1-
884 18,1990.

885 Rue, E.L. and Bruland, K.W.: Complexation of iron(III) by natural organic ligands in the
886 Central North Pacific as determined by a new competitive ligand equilibration /
887 adsorptive cathodic stripping voltametric method, *Mar. Chem.,* 50, 117–138, 1995.
888 Simmons, H.L., Jayne, S.R., St. Laurent, L.C. and Weaver, A.J.: Tidally-driven mixing in
889 a numerical model of the ocean general circulation, Ocean Modelling, 6, 245-263,
890 2004.
891 Strzepek, R.F. and Harrison, P.J.: Photosynthetic architecture differs in coastal and
892 oceanic diatoms, Nature, 431, 689-692, 2004.
893 Sunda, W.G. and Huntsman, S.A.: Interrelated influence of iron, light, and cell size on
894 marine phytoplankton growth, Nature, 390, 389-392, 1997.
895 Tagliabue, A., and Arrigo, K.R.: Iron in the Ross Sea: 1. Impact on CO_2 fluxes via
896 variation in phytoplankton functional group and non-Redfield stoichiometry, J.
897 Geophys. Res., 110, C03009, doi:10.1029/2004JC002531, 2005.
898 Timmermans, K.R., van der Wagt, B. Veldhuis, M.J.W.,. Maatman, A.and De Baar,
899 H.J.W.: Physiological responses of three species of marine pico-plankton to
900 ammonium, phosphate, iron and light limitation, J. Sea Res., 53, 109-120, 2005.
901 Tortell, P.D., Maldonado, M.T., Granger, J. and Price, N.M.: Marine bacteria and
902 biogeochemical cycling of iron in the oceans, FEMS Microbio. Ecol., 29, 1-11, 1999.
903 Trick, C.G., Andersen, R.J., Price, N.M., Gillam, A. and Harrison, P.J.: Examination of
904 hydroxamate-siderophore production by neritic eukaryotic marine phytoplankton,
905 Mar. Biol., 75,9-17, 1983.

906 Weber, L., Volker, C., Schartau, M. and Wolf-Gladrow, D.: Modeling the
907 biogeochemistry and speciation of iron at the Bermuda Atlantic Time Series site,
908 Global Biogeochemical Cycles, 19, GB1019, 2005.
909 Wu, J., Boyle, E., W. Sunda, W. and. Wen, L.-S.: Soluble and colloidal iron in the
910 oligotrophic North Atlantic and North Pacific, Science, 293, 847-849, 2001.
911

Variable	*Description*	*Reference or* Initial guess	*Final Value*	*Units*
κ_{eppley}	Temperature dependence of growth	*0.063 (Eppley, 1972)*	0.063	deg C^{-1}
γ_{irr_mem}	Photoadaptation time constant	1	1	d^{-1}
P^c_0	Maximum carbon-specific growth rate at 0 C	1.00E-05	1.00E-05	s^{-1}
α_{max}	Quantum yield under low light, abundant iron	*6.4-100 (Geider, 1997)*	73.6	$\mu g\ C\ g^{-1}\ chl\ m^2\ W^{-1}\ s^{-1}$
α_{min}	Quantum yield under low light, extreme iron limitation	*6.4-100 (Geider, 1997)*	18.4	$\mu g\ C\ g^{-1}\ chl\ m^2\ W^{-1}\ s^{-1}$
$\theta_{max\text{-}hi}$	Maximum Chl:C ratio, abundant iron	*0.007-0.072 (Geider, 1997)*	0.04	g Chl g C^{-1}
$\theta_{max\text{-}lo}$	Maximum Chl:C ratio, extreme iron limitation	*0.007-0.072 (Geider, 1997)*	0.01	g Chl g C^{-1}
$\gamma_{biomass}$	Biomass adjustment time constant	0.5	0.5	d^{-1}
kFe	Dissolved Fe uptake half-saturation constant	0.8	0.8	nmol kg^{-1}
kPO_4	PO_4 uptake half-saturation constant	0.2	0.1	μmol kg^{-1}
$Fe:P_{max}$	Maximum Fe:P uptake ratio	4.24	2.968	mmol Fe mol P^{-1}
kFe:P	Half-saturation cellular Fe:P	1.06	0.742	mmol Fe mol P^{-1}
λ_0	Carbon-specific phytoplankton mortality rate	*0.19 (Dunne et al., 2005)*	0.19	d^{-1}
P*	Pivotal phytoplankton biomass	*0.018 (Dunne et al., 2005)*	0.018	μmol P kg^{-1}
κ_{remin}	Temperature dependence of particulate production	*-0.032 (Dunne et al., 2005)*	-0.032	deg C^{-1}
ϕ_{DOP}	Fraction of non-particulate uptake converted to DOM	0.1	0.1	unitless (fraction)
γ_{DOP}	Decay timescale of DOM	0.25	0.25	y^{-1}
C:P	Carbon to Phosphorus ratio in organic matter	*106 (Anderson,1995)*	106	mol C mol P^{-1}
O_2:P	O_2:P for photosynthesis and respiration	*150 (Anderson,1995)*	150	mol O_2 mol P^{-1}
$wsink_{0z}$	Depth at which sinking rate starts increasing	80	80	m
$wsink_o$	Initial sinking rate	16	16	m d^{-1}
$wsink_{acc}$	Acceleration rate of sinking with depth	0.05	0.05	d^{-1}
γ_{POP}	Remineralization rate of sinking POM	0.12	0.12	d^{-1}
kO_2	Half-saturation constant for aerobic respiration	20	20	μmol kg^{-1}
$remin_{min}$	Minimum anaerobic respiration rate	0.3	0.3	unitless (fraction)
$O_{2\text{-}min}$	Minimum O_2 concentration for aerobic respiration	1	1	μmol kg^{-1}
Ligand	Ligand concentration	*1 (Parekh et al., 2005)*	1	nmol kg^{-1}
$Fe:P_{sed}$	Fe:P for sedimentary iron source	*.072 (Elrod et al., 2004)*	0.0106	mol Fe mol P^{-1}
$KFeL_{eq\text{-}max}$	Maximum Fe-ligand stability constant	*1e10-1e13 (Parekh et al., 2004)*	8.0E+10	kg mol lig^{-1}
$KFeL_{eq\text{-}min}$	Minimum Fe-ligand stability constant	4.00E+10	8.0E+09	kg mol lig^{-1}
$KFeL_{eq\text{-}irr}$	Irradiance scaling term for Kfe	1	0.10	W m^{-2}
$KFeL_{eq\text{-}Femin}$	Low-Fe threshold for reduced stability constant	0.05	0.05	nmol kg^{-1}
kFe_{org}	Organic-matter dependent scavenging rate	3	0.5	$gC^{-1}\ m^3\ d^{-1}$
kFe_{inorg}	Inorganic scavenging rate	3000	1000.00	d^{-1} nmol $Fe^{-.5}\ kg^{.5}$

Table 1: Parameters used in BLING for the experiments shown here. Reference values are given, where appropriate, in italics. Otherwise, the initial guess is shown.

Corr,*Reg* **Err**	All Mean	Varα	Varθ	Varα+ Varθ	Var Liebig	Varθ+ Liebig	Varα+ Liebig	AllVar
Annual Mean PO_4	0.74 *0.51* ***0.41***	0.85 *0.65* ***0.33***	0.85 *0.65* ***0.33***	0.90 *0.76* ***0.26***	0.94 *0.91* ***0.20***	0.93 *0.89* ***0.20***	0.93 *0.89* ***0.20***	0.93 *0.89* ***0.20***
Annually varying PO_4	0.71 *0.52* ***0.44***	0.81 *0.66* ***0.36***	0.81 *0.66* ***0.35***	0.88 *0.76* ***0.29***	0.92 *0.89* ***0.23***	0.91 *0.87* ***0.22***	0.91 *0.87* ***0.22***	0.91 *0.87* ***0.23***
Minimum PO_4	0.49 *0.28* ***0.48***	0.71 *0.50* ***0.37***	0.71 *0.50* ***0.37***	0.81 *0.68* ***0.27***	0.86 *0.92* ***0.18***	0.85 *0.93* ***0.19***	0.85 *0.93* ***0.19***	0.85 *0.93* ***0.19***
Annual Mean log(Chl)	0.92 *1.11*	0.87 *1.09*	0.94 *1.09*	0.87 *1.02*	0.92 *0.94*	0.94 *0.96*	0.84 *0.88*	0.86 *0.90*
Zonally-averaged PP (vs. Carr)	0.63	0.68	0.68	0.72	0.78	0.76	0.76	0.75
Zonally averaged PE (vs. Carr)	0.40	0.45	0.45	0.47	0.50	0.47	0.47	0.44

Table 2: Correlation, *regression* (italicized) coefficients and ***RMS errors*** (in bold) for the output of the model suite used here.

Figure 1: Conceptual map of the Biogeochemistry with Light Iron Nutrients and Gas model. Prognostic tracers are shown as squares with solid outlines. Relevant environmental state variables are shown as circles. Diagnostic quantities are shown as squares with dashed outlines, where Chl is chlorophyll and Biom is biomass. The suite of plankton growth calculations are represented by the green oval. Solid lines show fluxes of prognostic quantities. Dashed lines (terminated by filled circles) indicate important interdependencies, with the arrow pointing toward the dependent variable.

Figure 2: Photosynthesis rate at 20 °C as a function of light intensity (I), for a variety of nutrient availabilities, with all three iron dependent terms. The heavy solid line represents PO_4 and Fe replete conditions. Other solid lines show PO_4 replete photosynthesis rates at two limiting Fe concentrations, while dashed lines show Fe replete photosynthesis rates at two limiting PO_4 concentrations. The dotted line shows photosynthesis rates when both PO_4 and Fe are limiting. Note that the approach to light-saturated photosynthesis rates is more gradual when iron is limiting, due to the reduction of photosynthetic efficiency.

Figure 3: Particle fluxes in the BLING model. (a) Profile of particle flux compared with Martin et al. (1987) and OCMIP2 particle flux curves. (b) Log of remineralization rate (% production/m) compared with previous work. (c) Ratio of sinking particulate material to primary production using this formulation, compared with observations from Dunne et al. (2005).

Figure 4: Macronutrient simulation in BLING (AllVar experiment). (a) Annual mean PO_4 concentration from model. (b) Annual mean average macronutrient concentration from observations (WOA01). (c) Annual range of PO_4 concentrations, 1 s.d., from model. (d) Annual range of average macronutrient concentration from observations (WOA01).

Figure 5: Surface chlorophyll, in mg/m^3, simulated by BLING (AllVar experiment) compared with satellite observations. (a) Annual mean chlorophyll, from model. (b) Observed chlorophyll, from SeaWifs (average). (c) Annual cycle of zonally averaged chlorophyll, model. (d) Annual cycle of zonally averaged chlorophyll, SeaWifs climatology (average). Note that the SeaWifs zonal average includes coastal regions with high chlorophyll concentrations, not captured by the model, which is therefore biased low.

Figure 6: Iron simulation in the BLING model (AllVar experiment). (a) Annual average surface iron concentration in nM. Symbols from the compilation of Moore and Braucher (2008), and represent discrete measurements, rather than annual averages. (b) Annual range of modeled iron concentrations, in nM (difference between local maximum and minimum). (c) Iron along the A16N section in the central Atlantic, symbols from the observations of Measures et al. (2008). (d) Annually averaged iron deficiency term Def_{Fe} (equation 4).

Figure 7: Comparison between modeled and satellite-based estimates of primary productivity and particle export (units of GtC/deg/yr) for AllVar (top panels) and the full

suite of experiments (lower panels). Plots show annually integrated values, correlations are for time varying values. (a,b) AllVar vs satellite-based estimates. (b) AllVar compared to the iron-dependency experiments, as described in the text.

Figure 8: Impact of including iron dependency terms on global, annual mean surface dissolved PO_4 concentrations (in μM). Panels a and g show simulated concentrations, whereas panels b-f and h show differences between the experiment indicated and the average macronutrient, calculated from observations (WOA01).

Figure 9: Impact of including iron dependency terms on light limitation (where 1 is no light limitation), vertically-weighted by phosphorus uptake rates. Panels a and f show simulated concentrations, whereas panels b-e and g show differences between the experiment indicated and the AllMean experiment, such that red colours indicate less light-limitation then AllMean, while blue colours indicate more-light limitation.

Figure 10: Impact of including iron dependency terms on growth rates, vertically-weighted by phosphorus uptake rates. Panels a and f show simulated rates (d^{-1}), whereas panels b-e and g show differences between the experiment indicated and the AllMean experiment as a ratio, such that red colours indicate faster growth rates and blue colours indicate slower growth rates.

Figure 11: Impact of including iron dependency terms on the seasonal cycles of export production at 80m and surface chlorophyll. (a) Particle export in GtC/yr, subpolar North

989 Atlantic (70W-0W,50-65N). Annually integrated values shown in parentheses. (b)
990 Surface chlorophyll in mg/m^3, subpolar North Atlantic. (c) Particle export in GtC/yr,
991 subpolar/polar Southern Ocean (80S-50S). Annually integrated values shown in
992 parentheses. (d) Surface chlorophyll in mg/m^3, subpolar Southern Ocean.
993
994 **Figure 12**: Interactive effects of photosynthetic terms on global carbon export production
995 (vertical flux at 100m). (a) The linear sum of changes caused by photosynthetic
996 efficiency terms and the light-saturated photosynthesis term, i.e. (Varα+θ - AllMean) +
997 (VarLiebig-AllMean). (b) The actual simulated change in export when all three terms are
998 simultaneously included, i.e. AllVar-AllMean. If the terms operated independently, the
999 two panels would be identical. Where the amplitude is reduced in (b) relative to (a), a
1000 decrease in the light-saturated photosynthesis rates is reducing the sensitivity to
1001 photosynthetic efficiency. Conversely, where changes in (b) are amplified relative to (a),
1002 an increase in light-saturated photosynthesis rates is enhancing the sensitivity to
1003 photosynthetic efficiency, so that the net result is larger than otherwise expected.

Galbraith et al. Figure 1

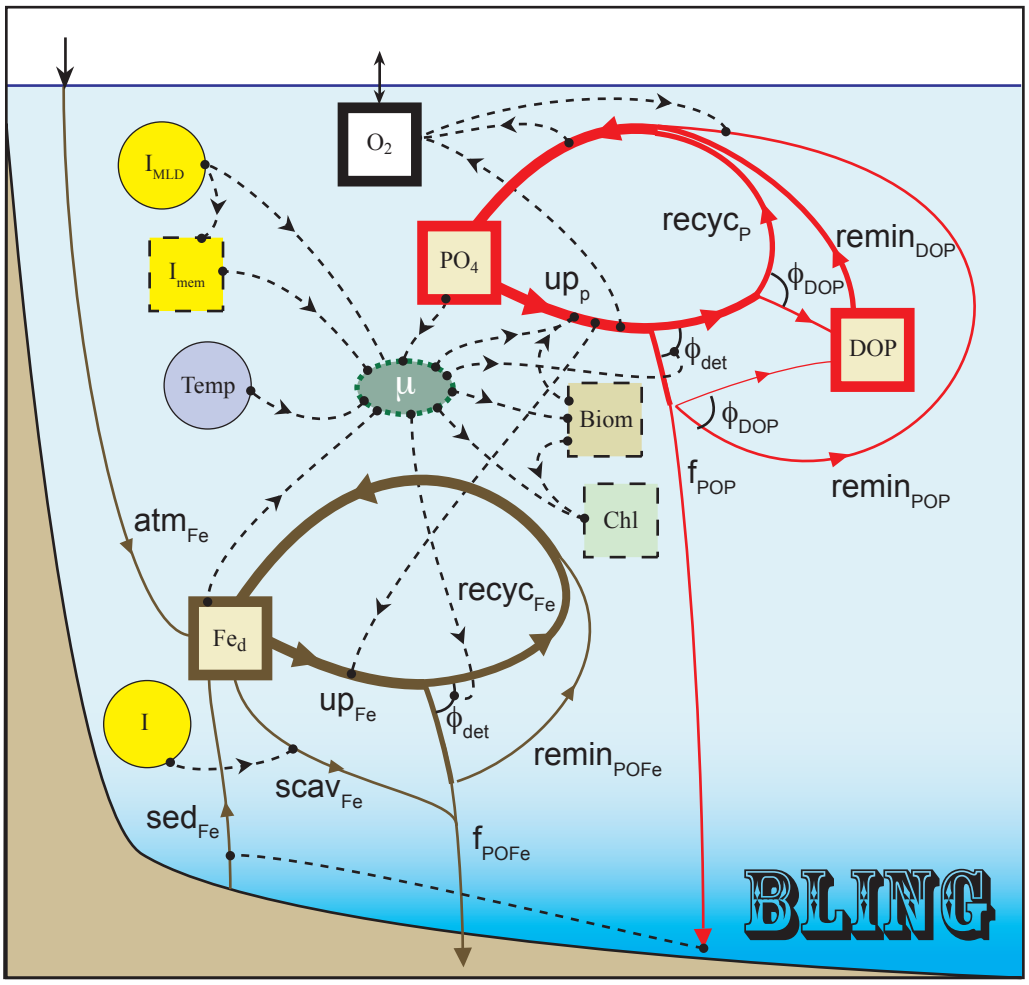

Galbraith et al. Figure 2

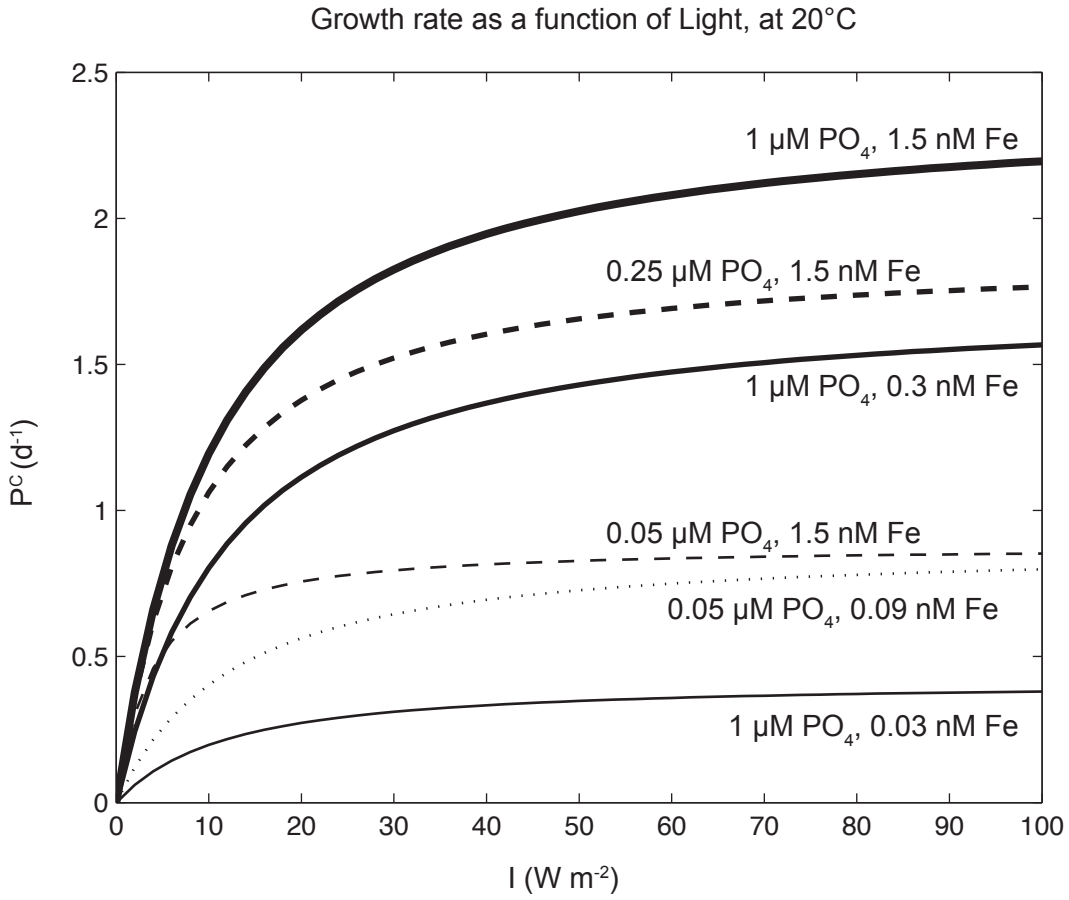

Galbraith et al. Figure 3

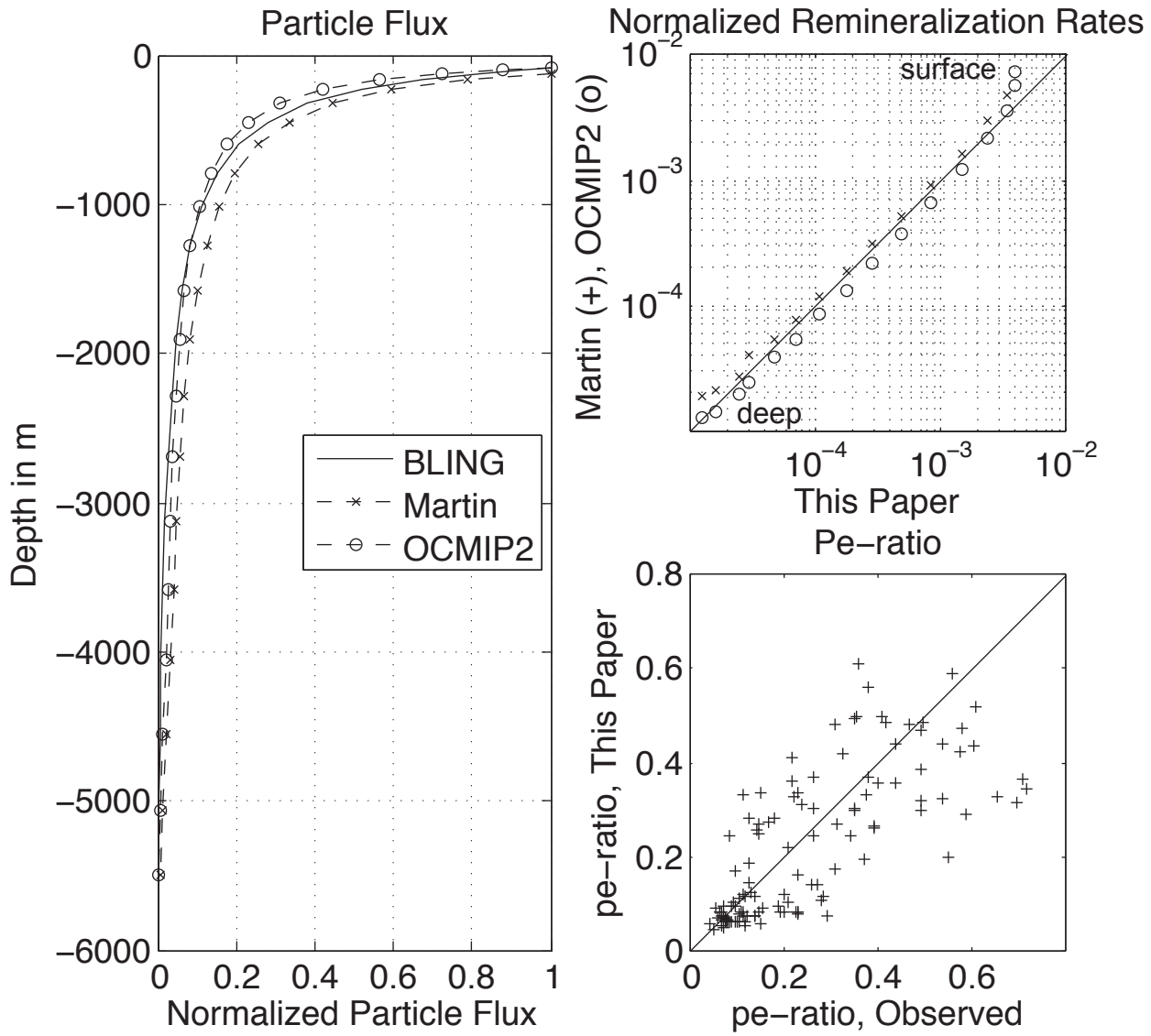

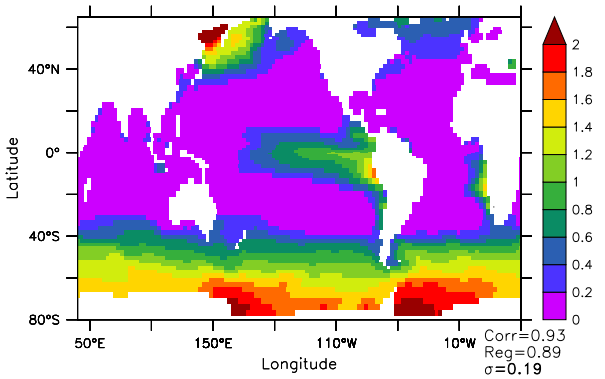

(a) Annual mean PO_4, model

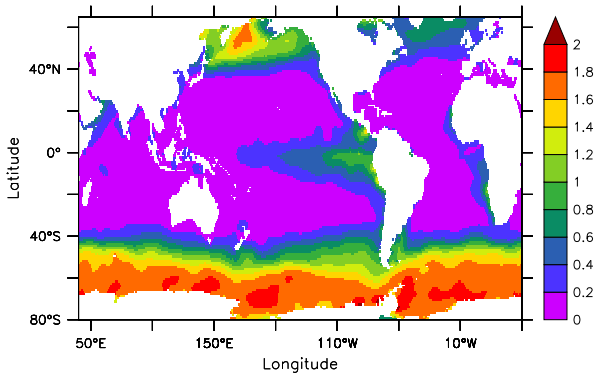

(b) Annual mean macronutrient, WOA01

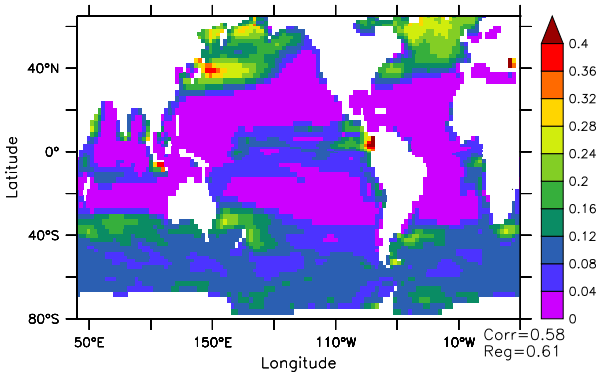

(c) Standard deviation PO_4, model

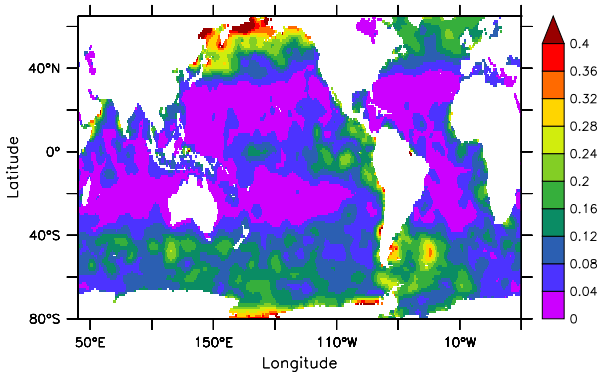

(d) Standard deviation macronutrient, WOA01

Galbraith et al. Figure 5

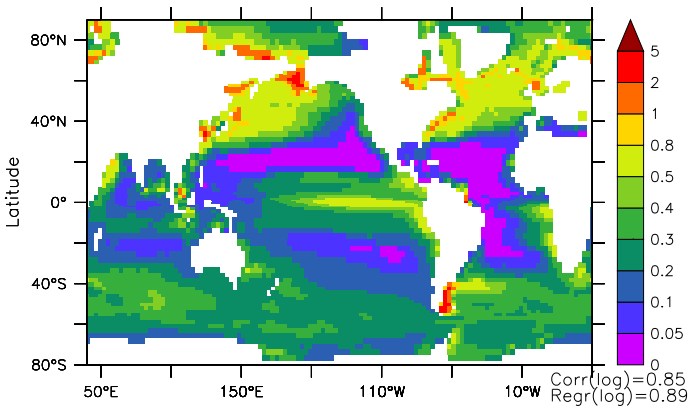

(a) Annual mean chlorophyll, model

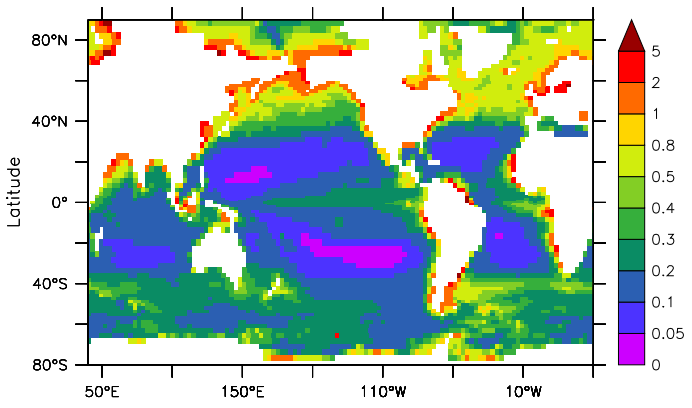

(b) Annual mean chlorophyll, SeaWIFS

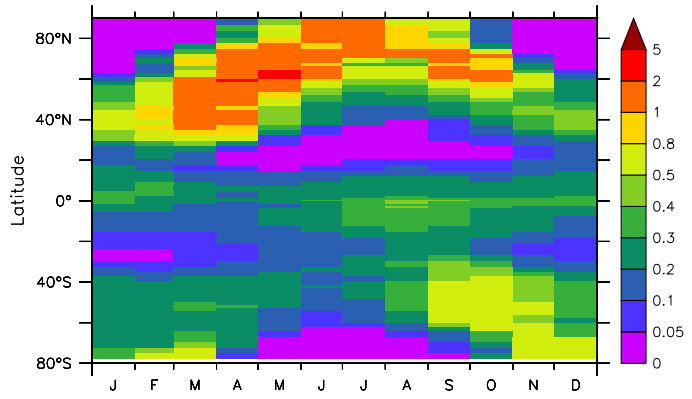

(c) Annual cycle of chlorophyll, model

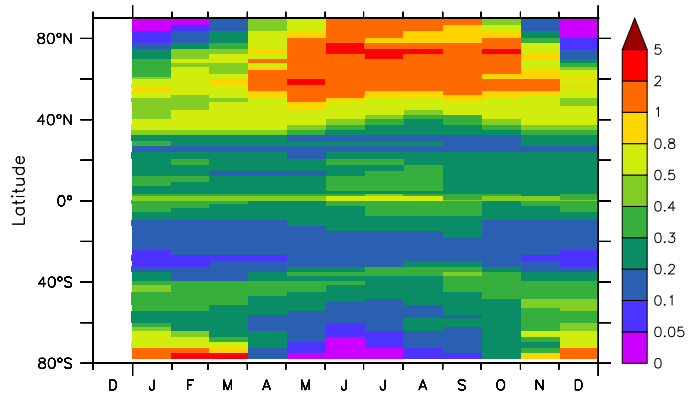

(d) Annual cycle of chlorophyll, SeaWIFS

Galbraith et al. Figure 6

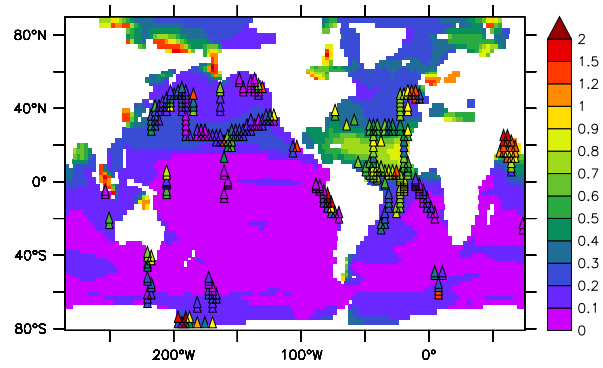

(a) Annual mean surface iron

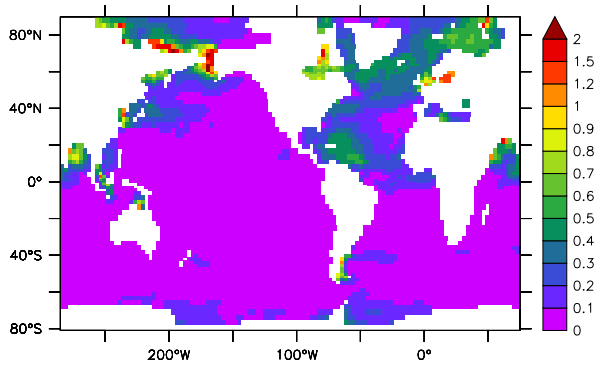

(b) Annual range of surface iron

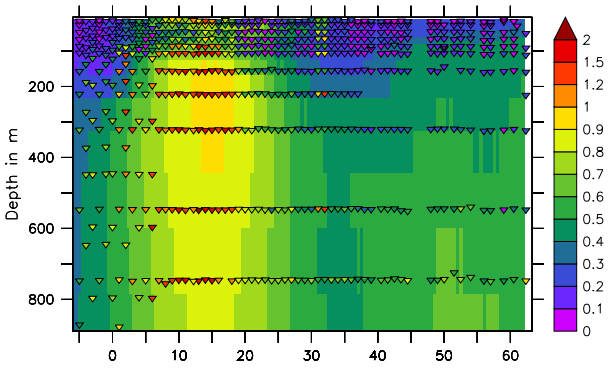

(c) Dissolved iron on A16N section

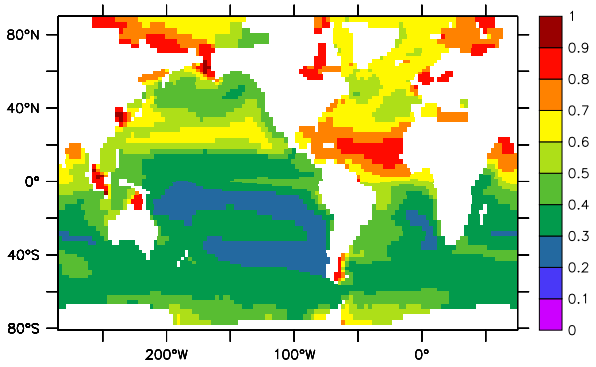

(d) Annual mean surface iron deficiency

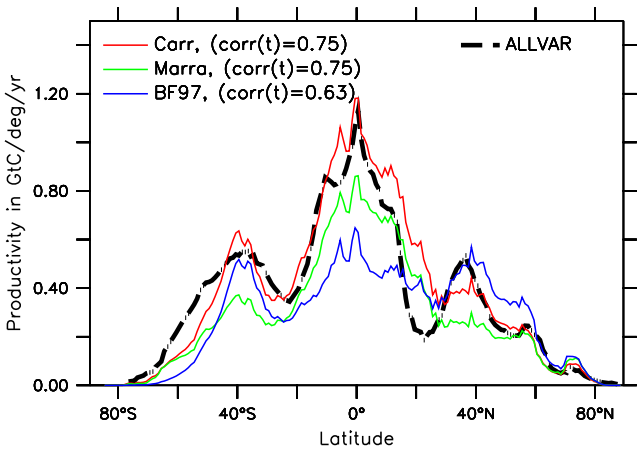

(a) Primary production vs. satellite

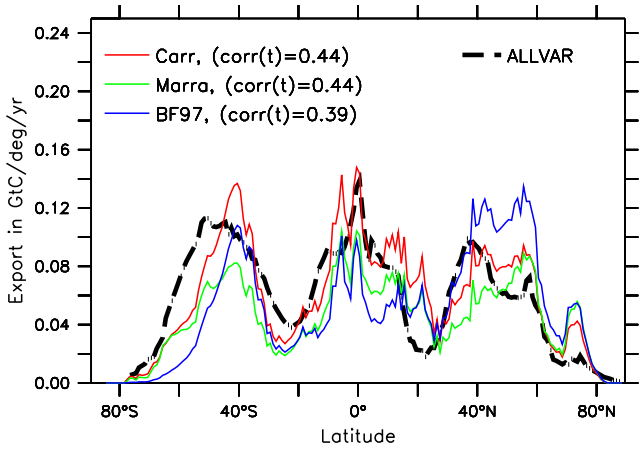

(b) Export production vs satellite

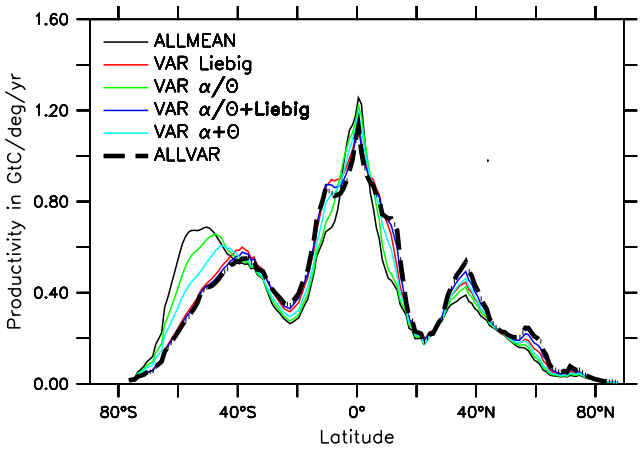

(c) Primary production, experiments

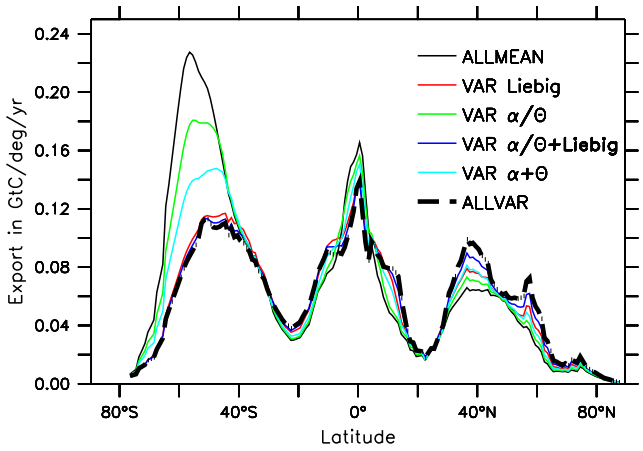

(d) Export production, experiments

Galbraith et al. Figure 8

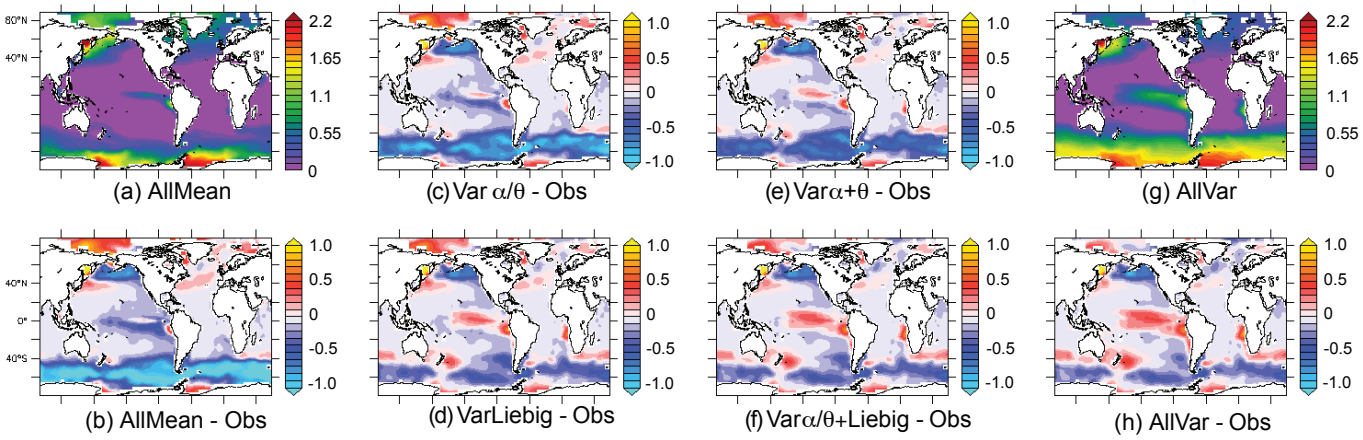

Galbraith et al. Figure 9

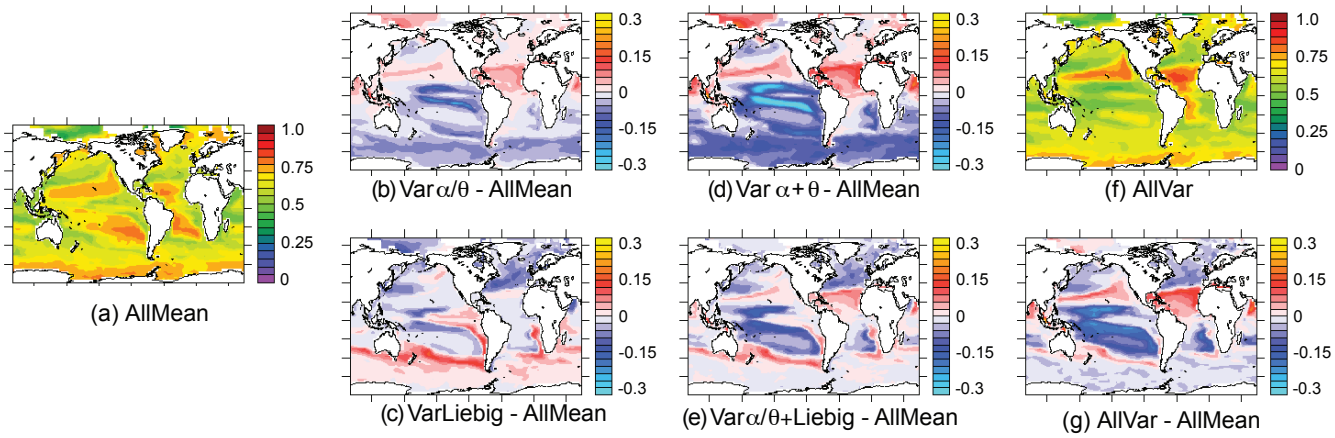

Galbraith et al. Figure 10

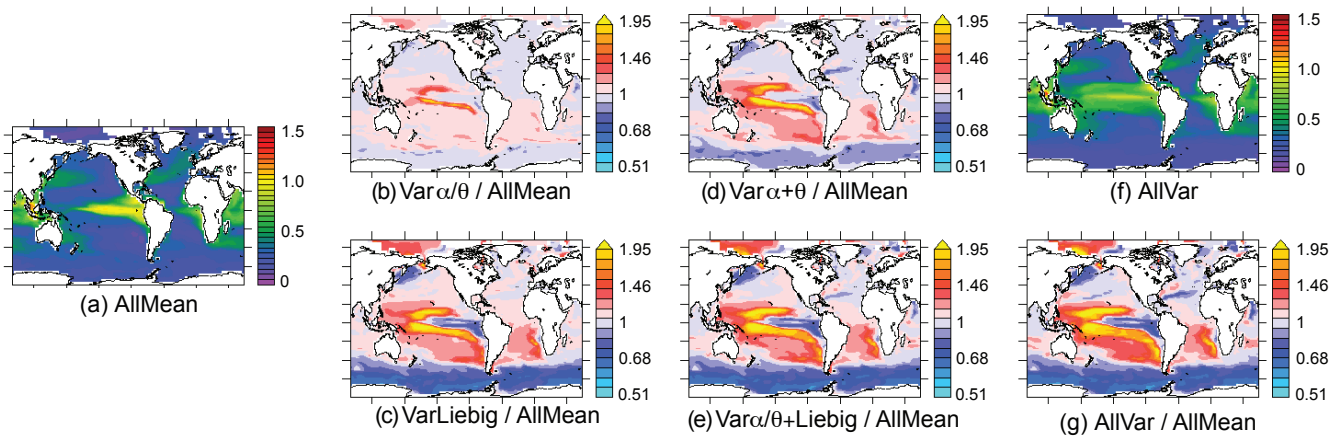

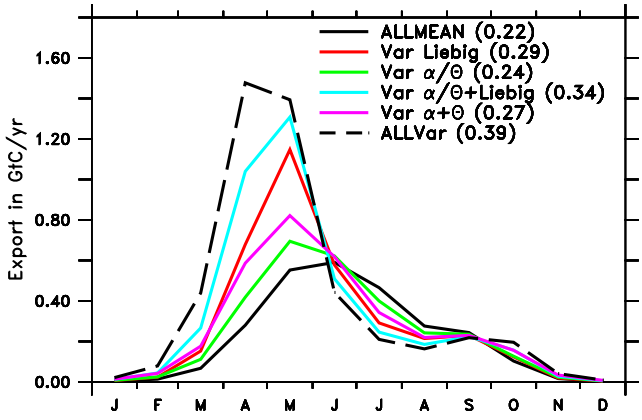

(a) N Atlantic export production

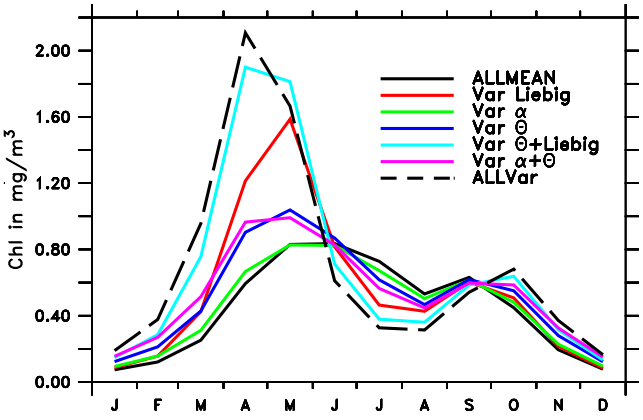

(b) N Atlantic surface chlorophyll

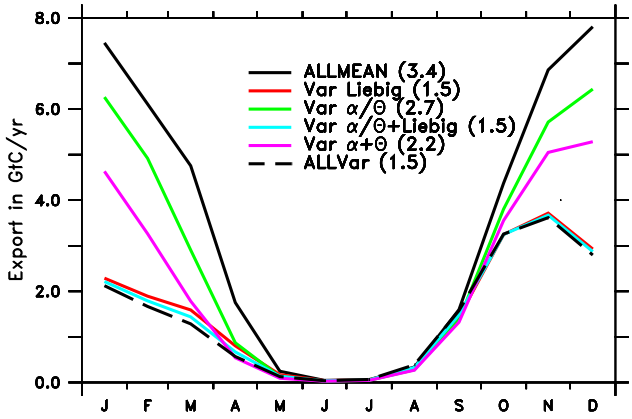

(c) Southern ocean export production

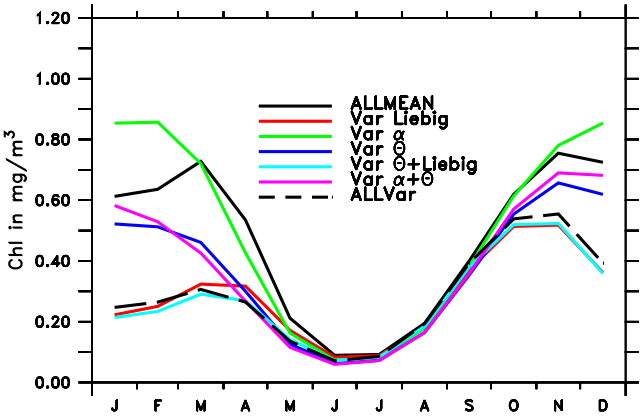

(d) Southern ocean surface chlorophyll

Galbraith et al. Figure 12

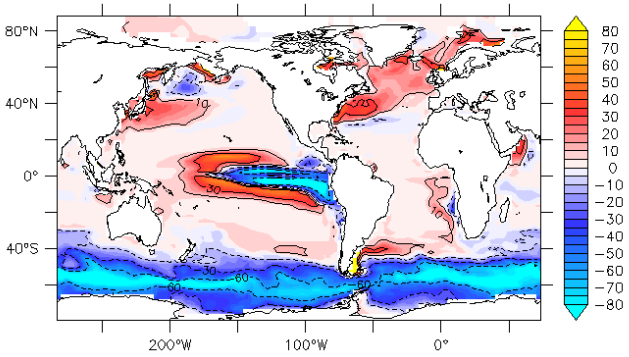

(a) Change in export, linear sum (g C m^{-2} a^{-1})

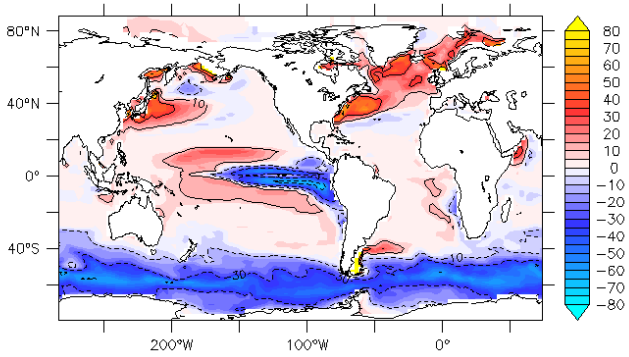

(b) Change in export, AllVar-AllMean (g C m^{-2} a^{-1})